Adhesion of graded elastic materials: A full self-consistent model and its application

Yudong Zhu [a], Zhijun Zheng [a,*], Chenguang Huang [b,c], Jilin Yu [a]

[a] *CAS Key Laboratory of Mechanical Behavior and Design of Materials, Department of Modern Mechanics, University of Science and Technology of China, Hefei, 230026, China*
[b] *Key Laboratory for Mechanics in Fluid Solid Coupling Systems, Institute of Mechanics, Chinese Academy of Sciences, Beijing, 100190, China*
[c] *Hefei Institutes of Physical Science, Chinese Academy of Sciences, Hefei, 230031, China*

ARTICLE INFO

ABSTRACT

A full self-consistent model (FSCM) of the axisymmetric adhesive contact between a rigid punch with an arbitrary surface shape and a power-law graded elastic half-space is developed. The self-consistent equation between the surface gap and the surface interaction (e.g., the Lennard–Jones force law) involves a nonlinear singular integral, posing a great challenge to numerical calculations. By applying the properties of Gauss's hypergeometric function, the integral singularity is eliminated in the numerical calculation through Riemann–Stieltjes integral. Case studies for power-law punch profiles are performed and the self-consistent equation can be expressed in a dimensionless form with three dimensionless parameters, namely a shape index, a gradient exponent, and a new generalized Tabor number. The FSCM results are obtained by solving the self-consistent equation through the surface central gap control method and Newton–Raphson iterative method. For large generalized Tabor numbers, the force–displacement curves are 'S-shaped' and condense to the extended JKR limit in the high-load branch. As the generalized Tabor number decreases, a continuous transition from the extended JKR model to the Bradley model for the adhesion of power-law graded materials is obtained. It is found that the pull-off force of a graded material usually depends on the three dimensionless parameters, but for some cases of the shape index, it is not sensitive to the gradient exponent when the generalized Tabor number is fixed. Asymptotic solutions are derived to predict the unstable jump points, which coincide well with the FSCM predictions. The FSCM is applied to validate the extended Maugis–Dugdale (M–D) model of graded materials and it is found that the accuracy of the original M–D-*n-k* model using the maximum strength condition to determine the cohesive stress is limited. By introducing the rigid-limit-consistency condition of the pull-off force to determine the cohesive stress, the M–D-*n-k* model is improved and its predictions show good consistency with the FSCM results.

1. Introduction

Surface adhesion exists extensively in biological systems and plays an important role in micro/nanoscopic contact mechanics (Arzt et al., 2003; Gao and Yao, 2004). Previous studies on some biological adhesion systems, e.g., gecko toes and spider hair, have shown that graded materials may have better adhesion properties in terms of robustness (flaw-tolerance) and stability than homogeneous ones (Yao and Gao, 2007; Flenner et al., 2020; Dong et al., 2020). In the framework of continuum mechanics, several

simplified theoretical models have been developed to characterize the adhesive contact behavior of graded materials (Giannakopoulos and Pallot, 2000; Chen et al., 2009a,b; Jin et al., 2013, 2021). However, with the rapid development of bio-inspired material design and fine surface measurement techniques, high expectations have been raised for the accuracy and applicability of adhesive contact models.

The adhesive behavior of homogeneous solids has been well characterized in several contact models. The Hertz theory (Hertz, 1882) pioneered contact mechanics, while the Bradley model (Bradley, 1932) first introduced the adhesion between two rigid spheres. In the 1970s, two elastic adhesive contact models, namely the Johnson–Kendall–Roberts (JKR) model (Johnson et al., 1971) and the Derjaguin–Muller–Toporov (DMT) model (Derjaguin et al., 1975) were proposed. Due to the difference in predicting the maximum adhesive force (pull-off force), these models have caused intense debate. In fact, there is a transition of pull-off force associated with a dimensionless parameter, known as the Tabor number (Tabor, 1977)

$$\mu = \left(\frac{R \Delta \gamma^2}{E^{*2} z_0^3} \right)^{1/3}, \tag{1}$$

where R is the sphere radius, $\Delta\gamma$ is the interface energy per unit area, z_0 is the characteristic length of the surface interaction range, and E^* is the equivalent elastic modulus of a homogeneous solid. The JKR model is suitable for large Tabor numbers (soft material and strong adsorption), while the DMT/Bradley model is appropriate for small Tabor numbers (hard material and weak adsorption). This JKR–Bradley transition was successfully characterized by a full self-consistent model (FSCM) (Hughes and White, 1979; Muller et al., 1980; Greenwood, 1997; Feng, 2000). The FSCM adopts a self-consistent relationship between the surface interaction and gap, making it the most accurate model of adhesive contact in the framework of continuum mechanics. Another form of the transition of pull-off force, known as the JKR–DMT transition, was derived from the Maugis–Dugdale (M–D) model (Maugis, 1992), with the Maugis number being the transition parameter, defined as

$$\lambda = \sigma_0 \left(\frac{9R}{2\pi \Delta \gamma E^{*2}} \right)^{1/3}, \tag{2}$$

where σ_0 is the cohesive stress. In the M–D model, the cohesive stress was usually considered to be equal to the theoretical stress (Maugis, 1992). This strategy is somewhat arbitrary and may greatly affect the prediction accuracy of the model. An alternative strategy to determine the value of the cohesive stress, namely *the rigid-limit-consistency condition*, was introduced by Zheng and Yu (2007b) when extending the M–D model to an arbitrary power-law profile, denoted as the M–D-*n* model with *n* being the shape index. The M–D-*n* model was recovered by using a harmonic potential function method (Zhou et al., 2011), and was validated by finite element simulation and experimental results (Grierson et al., 2013).

The great success of the above adhesive models in dealing with the contact problems of homogeneous materials encourages researchers to apply them to understand the adhesion of graded materials. Among various kinds of graded materials, the materials with Young's modulus dependent on depth according to a power law, namely the power-law graded materials, have received great attention due to the convenience of theoretical analysis. The fundamental solutions of this type of material under point, line, and ring loadings were reported by Booker et al. (1985a,b). The Hertz solutions of the contact between axisymmetric rigid indenters and the power-law graded materials were presented by Giannakopoulos and Suresh (1997a,b). These solutions shed light on the study of adhesive contact of power-law graded solids.

Based on the above fundamental solutions, a frictionless JKR model of power-law graded materials, namely the JKR-*k* model with *k* being the gradient exponent of Young's modulus, was developed for the plain strain (Giannakopoulos and Pallot, 2000; Chen et al., 2009a) and axisymmetric (Chen et al., 2009b) adhesive contact problems. The JKR-*k* model was further extended to the non-slipping cases (Jin and Guo, 2010, 2012; Guo et al., 2011) and the rough surface cases (Jin and Guo, 2013; Jin et al., 2016). Li and Popov (2018) adopted a boundary element method and used an energy balance condition identical to the JKR theory to study the adhesion of power-law graded materials. It is expected that all these JKR-type models are valid only for soft material and strong adsorption.

In response to the limitation of JKR-type models, Jin et al. (2013) extended the classical double-Hertz model developed by Greenwood and Johnson (1998) and predicted the JKR–DMT transition of power-law graded materials. In addition, Willert (2018) applied the method of dimensionality reduction to the adhesive contact of power-law graded materials and obtained the M–D solutions of arbitrary surface shapes, namely the M–D-*k* model. Recently, Jin et al. (2021) adopted another method based on the principle of superposition to derive the M–D-*k* model, and they applied the M–D-*k* solutions to the special case of power-law punch profiles and obtained the M–D-*n-k* model. It should be noted that there is an apparent difference in the force–displacement curves as well as the pull-off forces when comparing the M–D-*n-k* and finite element results, as shown in Figs. 5 and 6 of Jin et al. (2021). This indicates that the M–D-*n-k* model is not accurate enough and needs to be improved.

This study aims to establish a much accurate adhesive contact model for the power-law graded materials and apply it to verify the M–D-*n-k* model. In Section 2, an FSCM for the power-law graded materials is established and the corresponding numerical calculation procedure is provided. In Section 3, the main results of the FSCM, including the force–displacement curves, the JKR–Bradley transition, the jumping-in/out instabilities, the surface deformation, and the pressure distribution, are analyzed. In Section 4, the M–D-*n-k* model is validated and improved. Conclusions are presented in Section 5.
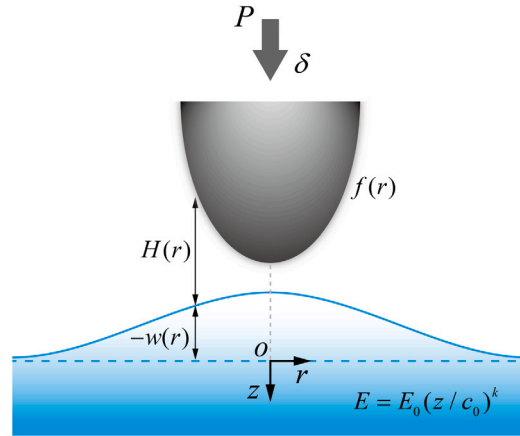
Fig. 1. Schematic representation of the frictionless adhesive contact between an axisymmetric rigid punch and a power-law graded elastic half-space.

2. Theoretical modeling and numerical calculation

2.1. A full self-consistent model

The frictionless adhesive contact between an axisymmetric rigid punch with its surface shape described by $f(r)$ and a power-law graded elastic half-space is considered, as shown in Fig. 1. The power-law graded elastic material is usually assumed to have a constant Poisson's ratio v and a Young's modulus E varying with depth z according to (Booker et al., 1985a,b; Giannakopoulos and Suresh, 1997a,b)

$$E = E_0(z/c_0)^k, \quad 0 < k < 1, \tag{3}$$

where E_0 is the reference modulus, c_0 is the characteristic depth and k is the gradient exponent. During contact, the gap between the punch and the half-space at radius r is given by

$$H(r) = -\delta + f(r) + w(r), \tag{4}$$

where δ denotes the relative displacement of distant points in the two objects and $w(r)$ is the surface deformation of the power-law graded elastic half-space.

For a determined interface pressure distribution $p(r)$, the surface deformation $w(r)$ can be calculated by

$$w(r) = \int_0^\infty p(t) w_\mathrm{u}(r,t)\,\mathrm{d}t, \tag{5}$$

where $w_\mathrm{u}(r,t)$ is the surface displacement under a ring loading with an intensity of unit pressure per unit length at the circle of $r = t$ (the subscript u represents 'unit'). The analytical solution of $w_\mathrm{u}(r,t)$ for the power-law graded material has been derived by Booker et al. (1985b), written as

$$w_\mathrm{u}(r,t) = \begin{cases} \dfrac{2bc_0^k}{E^* t^k}\,_2\mathrm{F}_1(\dfrac{k+1}{2}, \dfrac{k+1}{2}; 1; \dfrac{r^2}{t^2}), & 0 \le r < t \\[2ex] \dfrac{2btc_0^k}{E^* r^{k+1}}\,_2\mathrm{F}_1(\dfrac{k+1}{2}, \dfrac{k+1}{2}; 1; \dfrac{t^2}{r^2}), & r \ge t \end{cases} \tag{6}$$

where $_2\mathrm{F}_1(\cdot)$ is the Gauss's hypergeometric function (its definition and some properties are given in Appendix A, and some inferences are derived in Appendices B and C), $E^* = E_0/(1 - v^2)$ is the equivalent elastic modulus and b is a parameter defined as

$$b = \frac{2^{k+1}(k+2)q\sin(q\pi/2)}{k(k+1)\mathrm{B}(k/2, 1/2)}\mathrm{B}(\frac{3+k+q}{2}, \frac{3+k-q}{2}), \quad q = \sqrt{(1+k)\left(1 - \frac{kv}{1-v}\right)}, \tag{7}$$

in which $\mathrm{B}(\cdot)$ is the Euler's beta function. The piecewise functions in Eq. (6) are inconvenient for numerical calculation. It is interesting to find that the piecewise functions can be rewritten as a unified formula by using the Kummer's quadratic transformation formulas (see Appendix B)

$$w_\mathrm{u}(r,t) = \frac{2btc_0^k}{E^*(r+t)^{k+1}}\,_2\mathrm{F}_1(\frac{k+1}{2}, \frac{1}{2}; 1; \frac{4rt}{(r+t)^2}). \tag{8}$$

The Derjaguin approximation (Derjaguin, 1934; Greenwood, 1997, 2007, 2009) is adopted to describe the interface interaction, which assumes that the force between two curved and inclined surfaces is identical to that between two plane and parallel surfaces

and its value depends on the local surface gap, i.e.,

$$p(r) = p_s(H(r)). \tag{9}$$

If the 12–6 Lennard–Jones (L–J) potential is adopted between any two atoms, the interface interaction between two flat and parallel homogeneous half-space is given by Barber (2018)

$$p_s(H) = \frac{8\Delta\gamma}{3z_0}\left[\left(\frac{H}{z_0}+1\right)^{-9} - \left(\frac{H}{z_0}+1\right)^{-3}\right], \tag{10}$$

where $\Delta\gamma$ is the interface energy per unit area and z_0 is the characteristic length of the surface interaction range. For graded materials, the interface interaction may not be expressed in an analytical form and should be determined from molecular dynamics simulation or experimental tests. For simplicity, the 9–3 force law is taken as an example in the present study to approximately describe the interface interaction of power-law graded materials, which has also been used in finite element simulation (Jin et al., 2013, 2021). More accurate force law can also be considered and the entire analytical framework in this study remains valid for power-law graded materials. In the Derjaguin approximation, the interface interaction is assumed to be along the axial direction, and the radial traction is ignored (Greenwood, 2009). Then, the total applied load P can be given by

$$P = \int_0^\infty p_s(H(r))2\pi r\,\mathrm{d}r. \tag{11}$$

Substituting Eqs. (5), (8) and (9) into Eq. (4) yields the self-consistent equation for the adhesive contact of the power-law graded elastic materials

$$H(r) = -\delta + f(r) + \frac{2bc_0^k}{E^*}\int_0^\infty p_s(H(t))\frac{t}{(r+t)^{k+1}}\,{}_2F_1(\frac{k+1}{2},\frac{1}{2};1;\frac{4rt}{(r+t)^2})\mathrm{d}t. \tag{12}$$

For the full self-consistent model, the great challenge is to solve this nonlinear relation involved with integral singularity.

In the limit of $k \to 0$, we have $b = 1$ and (see Appendix A)

$${}_2F_1(\frac{1}{2},\frac{1}{2};1;\frac{4rt}{(r+t)^2}) = \frac{2}{\pi}K(\frac{2\sqrt{rt}}{r+t}), \tag{13}$$

and Eq. (12) can be reduced to

$$H(r) = -\delta + f(r) + \frac{4}{\pi E^*}\int_0^\infty p_s(H(t))\frac{t}{r+t}K(\frac{2\sqrt{rt}}{r+t})\mathrm{d}t, \tag{14}$$

where $K(\cdot)$ denotes the complete elliptic integral of the first kind. Eq. (14) is the classical self-consistent equation for the adhesion of homogeneous solids used in the extensive literature (Muller et al., 1980; Greenwood, 1997; Feng, 2000; Zheng et al., 2007; Zhu et al., 2021).

2.2. Singularity elimination method

The adhesive contact solutions of power-law graded elastic materials can be acquired by solving the nonlinear integral equation (Eq. (12)) numerically. But, there is a tough flaw that the Gauss's hypergeometric function ${}_2F_1(\cdot)$ in Eq. (12) is singular at $t = r$. This integral singularity may reduce the accuracy of numerical integration. When solving the reduced equation corresponding to homogeneous material, i.e., Eq. (14), Muller et al. (1980) and Attard and Parker (1992) did not discuss the singular point, Greenwood (1997) and Papangelo and Ciavarella (2020) dealt with the singular point through the overlapping triangles method, and Feng (2000) considered the singular point through approximate integral. However, these approximations may limit the accuracy of numerical integration and the efficiency of numerical solving.

In contrast to the approximate methods, Zheng et al. (2007) developed an exact method to deal with the integral singularity in the adhesion problem of homogeneous material. The primitive function of $K(\cdot)$ was introduced and the integral singularity at $t = r$ is avoided (see Appendix D), which was also adopted in our recent work (Zhu et al., 2021). A function with respect to s is given by (Zhu et al., 2021; Zheng et al., 2007)

$$\Phi_0(s) = \frac{1}{\pi}\left[(s-1)K(\frac{2\sqrt{s}}{1+s}) + (1+s)E(\frac{2\sqrt{s}}{1+s})\right], \tag{15}$$

and its derivative is written as

$$\frac{\mathrm{d}\Phi_0(s)}{\mathrm{d}s} = \frac{2s}{\pi(1+s)}K(\frac{2\sqrt{s}}{1+s}), \tag{16}$$

where the subscript 0 represents the homogeneous material ($k = 0$), and $E(\cdot)$ denotes the complete elliptic integral of the second kind. By using Eqs. (15) and (16) with $s = t/r$, Eq. (14) can be rewritten as

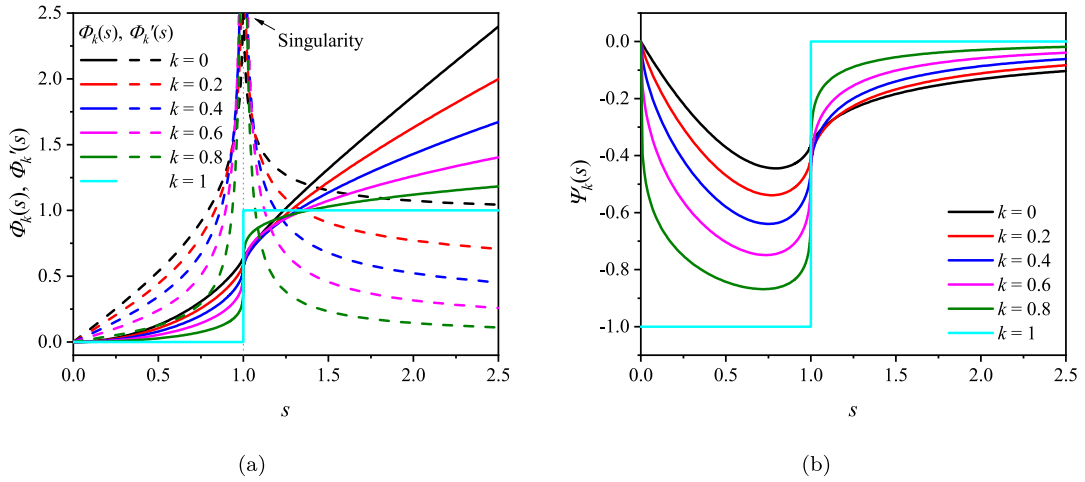$$H(r) = -\delta + f(r) + \frac{2r}{E^*}\int_{t=0}^{t=\infty} p_s(H(t))\mathrm{d}\Phi_0(t/r). \tag{17}$$

Fig. 2. (a) The function $\Phi_k(s)$ and its derivative $\Phi'_k(s)$ and (b) the function $\Psi_k(s)$ for some values of gradient exponent k.

In numerical calculation, applying the Riemann–Stieltjes integral method to Eq. (17) can avoid the issue of integral singularity (Zheng et al., 2007; Zhu et al., 2021).

Inspired by the strategy used in the adhesion problems of homogeneous material (Zheng et al., 2007; Zhu et al., 2021), we can derive a new function $\Phi_k(s)$ via rigorous mathematical derivation to avoid the integral singularity at $t = r$ for power-law graded elastic materials, given by (see Appendix E)

$$\Phi_k(s) = \frac{1}{2(1+s)^k}\left[(s-1)\,{}_2\mathrm{F}_1(\frac{k+1}{2},\frac{1}{2};1;\frac{4s}{(1+s)^2}) + (1+s)\,{}_2\mathrm{F}_1(\frac{k-1}{2},\frac{1}{2};1;\frac{4s}{(1+s)^2})\right].$$ (18)

The derivative of $\Phi_k(s)$ with respect to s can be derived as (see Appendix E)

$$\frac{\mathrm{d}\Phi_k(s)}{\mathrm{d}s} = \frac{(1-k)\,s}{(1+s)^{1+k}}\,{}_2\mathrm{F}_1(\frac{k+1}{2},\frac{1}{2};1;\frac{4s}{(1+s)^2}).$$ (19)

The newly defined function $\Phi_k(s)$ (Eq. (18)) and its derivative $\Phi'_k(s)$ (Eq. (19)) are plotted in Fig. 2(a) for several special values of k. It is shown that $\Phi'_k(s)$ is singular at $s = 1$, but $\Phi_k(s)$ is a continuous function with respect to s for any case of $0 \leq k < 1$. Additionally, it can be seen from Fig. 2(a) that $\Phi'_k(s)$ becomes sharper around the point $s = 1$ with the increase of k. Hence, using an approximate method to deal with the integral singularity may cause a larger numerical error for power-law graded elastic materials ($0 < k < 1$) compared with the homogeneous one ($k = 0$). By using Eq. (19) with $s = t/r$, Eq. (12) can be rewritten as

$$H(r) = -\delta + f(r) + \frac{2bc_0^k r^{1-k}}{E^*(1-k)}\int_{t=0}^{t=\infty} p_{\mathrm{s}}(H(t))\mathrm{d}\Phi_k(t/r).$$ (20)

Definitely, the integral singularity for any case of $0 < k < 1$ can also be avoided.

Here, we make some discussion on the case of $r = 0$, which leads to $t/r \to \infty$ and $\Phi_k(t/r) \to \infty$ when $t > 0$. There is no need to consider the case of $t \to \infty$, because in this case $p_{\mathrm{s}}(H(t))$ approaches zero quickly. It is noticed that ${}_2\mathrm{F}_1(\alpha, \beta; \gamma; 4s/(1+s)^2) \to 1$ as $s \to \infty$ for arbitrary parameters α, β and γ, and for the case of a finite value of t and $r \to 0$, $\Phi_k(t/r)$ follows an asymptotic behavior

$$\Phi_k(t/r) \sim (t/r)^{1-k}.$$ (21)

Thus, we introduce another function $\Psi_k(s)$, defined as

$$\Psi_k(s) = \Phi_k(s) - s^{1-k},$$ (22)

and then Eq. (20) can be rewritten as

$$H(r) = -\delta + f(r) + \frac{2bc_0^k r^{1-k}}{E^*(1-k)}\int_{t=0}^{t=\infty} p_{\mathrm{s}}(H(t))\mathrm{d}\Psi_k(t/r) + \frac{2bc_0^k}{E^*(1-k)}\int_{t=0}^{t=\infty} p_{\mathrm{s}}(H(t))\mathrm{d}t^{1-k}.$$ (23)

The last term in Eq. (23) is independent of r and it is the surface deformation at the central point, i.e., $w(0)$. From Fig. 2(b), it is found that $\Psi_k(s)$ is bounded and continuous for $0 \leq s < \infty$, so the integral singularity at $r = 0$ is also eliminated. Fortunately, Eq. (23) gives the self-consistent equation for power-law graded elastic materials without any integral singularity. Therefore, we strongly recommend using Eq. (23) as the basic equation for numerical calculation. It should be noted that there is no restriction on the form of the interface interaction in the full self-consistent equation (Eq. (23)) for power-law graded materials. An exact interface interaction obtained from molecular dynamics simulation or experimental tests may be applied in Eq. (23) to improve the accuracy of the FSCM.

A numerical calculation method is introduced in this study for $0 \leq k < 1$. It is noticed that the numerical calculation may become difficult when $k \to 1$ because $\Psi_k(s)$ changes drastically around $s = 1$, which requires a fine mesh. The case of linear gradient ($k = 1$) is of great research interest. But for the limiting case of $k = 1$, the Poisson's ratio ν must be taken as $1/2$ to ensure that the term $b/(1 - k)$ in Eq. (23) is a finite value. The case of $k = 1$ and $\nu = 1/2$ is referred to as the Gibson limit (Chen et al., 2009a,b; Jin et al., 2013, 2021). It is noted that when $k \to 1$, $\Phi_k(s)$ and $\Psi_k(s)$ are both step functions, as illustrated in Fig. 2, and the self-consistent equation can be solved by using the properties of the step function and its derivative the delta function. For the convenience of comparison, the predictions in the case of Gibson solid ($k = 1$ and $\nu = 1/2$) will be presented in some figures below.

2.3. Nondimensionalization

Power-law punch profiles are taken as representative cases in this study. The shape function is described by (Zheng and Yu, 2007b)

$$f(r) = \frac{r^n}{nQ}, \tag{24}$$

where n is the shape index and Q is the shape parameter with the dimension of [length]$^{n-1}$. For $n = 1$, the punch profile is a cone, and Q is usually denoted as $\tan \phi$, with ϕ being the semiangle. For $n \neq 1$, Q is usually written as R^{n-1}, with R being a characteristic length. For example, $n = 2$ represents a paraboloid (or a near sphere), and $n \to \infty$ gives a flat punch.

For the adhesive contact problems between the power-law shaped punch and the power-law graded elastic materials, the longitudinal characteristic size is z_0 and the transverse characteristic size is $(Qz_0)^{1/n}$. Hence, the following dimensionless parameters can be introduced

$$\bar{H} = \frac{H}{z_0}, \quad \bar{\delta} = \frac{\delta}{z_0}, \quad \bar{r} = \frac{r}{(Qz_0)^{1/n}}. \tag{25}$$

The surface profile in a dimensionless form is given by

$$\bar{f}(\bar{r}) \equiv \frac{f(r)}{z_0} = \frac{\bar{r}^n}{n}, \tag{26}$$

and the dimensionless L–J function of surface interaction can be written as

$$\bar{p}_s(\bar{H}) \equiv \frac{p_s(H)}{\Delta\gamma/z_0} = \frac{8}{3} \left[(\bar{H} + 1)^{-9} - (\bar{H} + 1)^{-3} \right]. \tag{27}$$

By using the above parameters, the self-consistent equation (Eq. (23)) can be rewritten in a dimensionless form as

$$\bar{H}(\bar{r}) = -\bar{\delta} + \bar{f}(\bar{r}) + 2\mu^{(2n+k-1)/n} \left[\bar{r}^{1-k} \int_{\bar{t}=0}^{\bar{t}=\infty} \bar{p}_s(\bar{H}(\bar{t})) \mathrm{d}\Psi_k(\bar{t}/\bar{r}) + \int_{\bar{t}=0}^{\bar{t}=\infty} \bar{p}_s(\bar{H}(\bar{t})) \mathrm{d}\bar{t}^{1-k} \right], \tag{28}$$

where μ is a generalized Tabor number, defined as

$$\mu = \left[\frac{Q^{1-k} c_0^{nk} \Delta\gamma^n b^n}{E^{*n} z_0^{2n+k-1} (1-k)^n} \right]^{1/(2n+k-1)}. \tag{29}$$

Some reduced forms of μ have been given for special values of n and k in the literature, e.g., the case of $k = 0$ (Zheng and Yu, 2007b) and the case of $k = 0$ and $n = 2$ (Tabor, 1977). It is found that the dimensionless form of the self-consistent equation only contains three dimensionless parameters, namely the shape index n, the gradient exponent k, and the generalized Tabor number μ.

It should be pointed out that the generalized Tabor number μ defined here is slightly different from the one defined by Jin et al. (2021), which is denoted as μ_{Jin} for distinction, i.e.

$$\mu_{\mathrm{Jin}} \equiv \left(\frac{Q^{1-k} c_0^{nk} \Delta\gamma^n}{E^{*n} z_0^{2n+k-1}} \right)^{1/(2n+k-1)} = \mu \left(\frac{1-k}{b} \right)^{n/(2n+k-1)}. \tag{30}$$

For the two limiting cases of homogeneous materials ($k = 0$) and Gibson solid ($k = 1$, $\nu = 1/2$), we have $b/(1 - k) \to 1$ from Eq. (7), which leads to $\mu = \mu_{\mathrm{Jin}}$. For general cases ($0 < k < 1$), the two parameters are not identical. If one takes μ_{Jin} to obtain a dimensionless form of the self-consistent equation, four parameters (n, k, μ_{Jin} and b (or ν)) will be explicitly included in the equation. Therefore, the benefit of using μ defined in Eq. (29) instead of μ_{Jin} is that the dimensionless parameters controlling the present problem can be reduced from four to three. This means that the similarity model of the present problem only has three similarity parameters.

The Tabor number has been explained as a measure of the ratio of an elastic deformation to the range of surface force (Tabor, 1977). For the present problem, the elastic deformation at any place of the solid is affected by the gradient exponent, and the one used to define the generalized Tabor number cannot be strictly estimated. Undoubtedly, the Tabor number can be generalized in different ways, but a similarity model containing relatively few similarity parameters is expected. In this sense, we take the form in Eq. (29) as the generalized Tabor number, and for simplicity, it is referred to as the Tabor number in the following parts.

A dimensionless form of the external force is given by

$$\bar{P} \equiv \frac{P}{\pi Q^{2/n} \Delta\gamma z_0^{2/n-1}} = 2 \int_0^\infty \bar{p}_s(\bar{H}(\bar{r})) \bar{r} \mathrm{d}\bar{r}. \tag{31}$$

2.4. Computational implement

A suitable control method should be adopted to obtain the solutions of Eq. (28). The displacement control method does not work well, because the force–displacement curves might be 'S-shaped', and this method may cause non-convergence of numerical iterations around the jumping points, as shown in the case of $k = 0$ (Greenwood, 1997; Feng, 2000; Zheng et al., 2007). The arc-length control method can well trace the equilibrium path and provide all equilibrium states (Feng, 2000; Zhu et al., 2021), but using this method in the numerical calculation is time-consuming. According to the existing experience (Greenwood, 1997; Zheng et al., 2007), for the adhesive contact problems of smooth surfaces, the surface central gap control method works well as the arc-length method, and it can increase computational efficiency. Hence, the surface central gap control method is employed in this study.

In the surface central gap control method, the displacement $\bar{\delta}$ is parameterized by the surface central gap $\bar{H}_0 = \bar{H}(0)$ (Greenwood, 1997; Zheng et al., 2007). From Eq. (28), the surface central gap $\bar{H}(0)$ can be expressed as

$$\bar{H}_0 = -\bar{\delta} + 2\mu^{(2n+k-1)/n} \int_{\bar{t}=0}^{\bar{t}=\infty} \bar{p}_s(\bar{H}(\bar{t})) \mathrm{d}\bar{t}^{1-k}. \tag{32}$$

Thus, the displacement $\bar{\delta}$ is given by

$$\bar{\delta} = -\bar{H}_0 + 2\mu^{(2n+k-1)/n} \int_{\bar{t}=0}^{\bar{t}=\infty} \bar{p}_s(\bar{H}(\bar{t})) \mathrm{d}\bar{t}^{1-k}. \tag{33}$$

Substituting Eq. (33) into Eq. (28) leads to

$$\bar{H}(\bar{r}) = \bar{H}_0 + \bar{f}(\bar{r}) + 2\mu^{(2n+k-1)/n}\bar{r}^{1-k} \int_{\bar{t}=0}^{\bar{t}=\infty} \bar{p}_s(\bar{H}(\bar{t})) \mathrm{d}\Psi_k(\bar{t}/\bar{r}). \tag{34}$$

The present study considered the infinite indenters, and the effective integral domain is $[0, \bar{r}_{\max}]$, where $\bar{r}_{\max}$ is chosen as the value under which the surface interaction can be neglected. In our calculation, $\bar{r}_{\max}$ is set to make $\bar{f}(\bar{r}_{\max}) = 50$ (Zheng et al., 2007). The effective domain is discretized into N uniform segments $[\bar{r}_{j-1}, \bar{r}_j]$ and N nodes (besides $\bar{r}_0 = 0$) at position $\bar{r}_j, j = 1, 2, \ldots, N$. For the cases studied, the accuracy of the results is sufficient when N is as large as 2500.

The Newton–Raphson iterative method is employed to solve Eq. (34) for the N unknowns of $\bar{H}_i = \bar{H}(\bar{r}_i)$ when $\bar{H}_0$ is given. The Riemann–Stieltjes integral method is applied to deal with the integral term in Eq. (34). The residual $\bar{R}_i$ is defined as

$$\bar{R}_i = \bar{H}_i - \bar{H}_0 - \bar{f}(\bar{r}) - 2\mu^{(2n+k-1)/n}\bar{r}_i^{1-k} \sum_{j=1}^{N} \bar{p}_s(\bar{H}(\bar{\xi}_j)) \left(\Psi_k(\bar{r}_j/\bar{r}_i) - \Psi_k(\bar{r}_{j-1}/\bar{r}_i)\right), \tag{35}$$

where $i = 1, 2, \ldots, N$, and $\bar{H}(\bar{\xi}_j)$ is approximated by $\bar{H}(\bar{\xi}_j) = (\bar{H}_{j-1} + \bar{H}_j)/2$. For a given value of $\bar{H}_0$, the Newton–Raphson iterative method gives

$$\left\{\bar{H}_i^{m+1}\right\} = \left\{\bar{H}_i^m\right\} - \left[\bar{J}_{ij}^m\right]^{-1} \left\{\bar{R}_j^m\right\}, \tag{36}$$

where m represents the iteration step and $\bar{J}_{ij}$ is the Jacobi matrix

$$\bar{J}_{ij} = \frac{\partial \bar{R}_i}{\partial \bar{H}_j}. \tag{37}$$

The iteration continues until the maximum of $\left|\bar{H}_i^{m+1}/\bar{H}_i^m - 1\right|$ for $i = 1, 2, \ldots, N$ is less than a given small value, say 10^{-6} (Zheng et al., 2007). After $\bar{H}_i$ ($i = 1, 2, \ldots, N$) is determined, the displacement $\bar{\delta}$ and the load $\bar{P}$ can be calculated by

$$\bar{\delta} = -\bar{H}_0 + 2\mu^{(2n+k-1)/n} \sum_{j=1}^{N} \bar{p}_s(\bar{H}(\bar{\xi}_j)) \left(\bar{r}_j^{1-k} - \bar{r}_{j-1}^{1-k}\right), \tag{38}$$

$$\bar{P} = \sum_{j=1}^{N} \bar{p}_s(\bar{H}(\bar{\xi}_j)) \left(\bar{r}_j^2 - \bar{r}_{j-1}^2\right), \tag{39}$$

respectively. By changing $\bar{H}_0$ to $\bar{H}_0 - \Delta\bar{H}_0$ and repeating the above steps, the solutions of the new control step can be acquired. The initial value in each iteration step is given by the convergence solution of the previous control step. In the numerical calculation, $\bar{H}_0$ decreases from a large value (say 10) to a small value (say -0.1). All the equilibrium states can be obtained after finishing the calculation steps.

3. Results and discussion

3.1. Features of the force–displacement curve at a large Tabor number

We first considered a special case of the adhesive contact between a rigid sphere ($n = 2$) and the power-law graded material of $k = 0.4$ at a large Tabor number ($\mu = 3$), and compared the FSCM results with the JKR-*n-k* results (Chen et al., 2009b; Jin et al.,
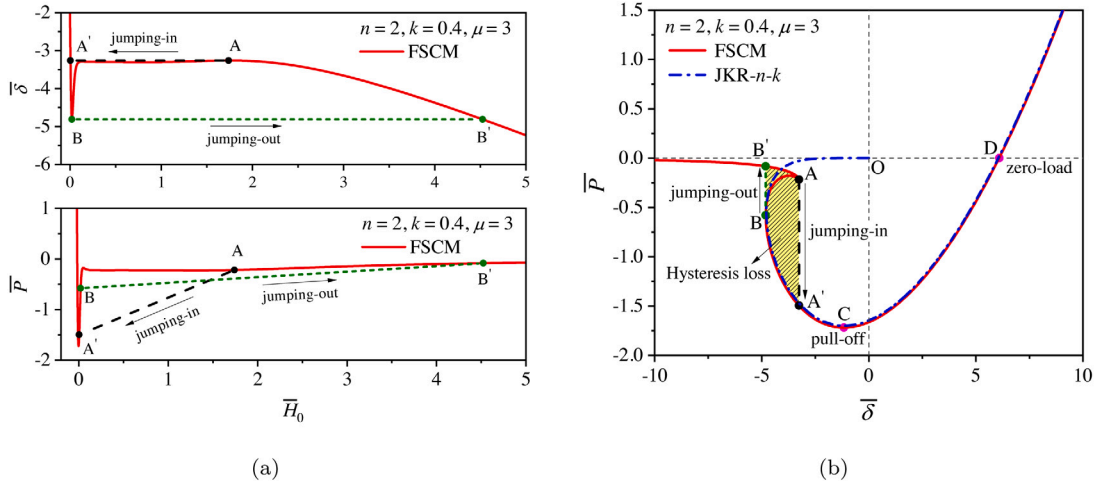
Fig. 3. (a) The displacement/force–surface central gap curves and (b) the force–displacement curve for $n = 2$, $k = 0.4$ and $\mu = 3$. The force–displacement curve predicted by the JKR-n-k model is also plotted in (b) for comparison.

2021). It is noted that in the following analysis, there is no need to specify the value of the Poisson's ratio ν because its effect has been included in our redefined Tabor number μ.

The displacement–surface central gap ($\bar{\delta}$ vs. $\bar{H}_0$), the force–surface central gap ($\bar{P}$ vs. $\bar{H}_0$) and the force–displacement ($\bar{P}$ vs. $\bar{\delta}$) curves are given in Fig. 3. It can be seen from Fig. 3(a) that both $\bar{P}$ and $\bar{\delta}$ are single-valued functions of $\bar{H}_0$, indicating that the surface central gap control method is available for the present problem. For large values of $\bar{H}_0$, $\bar{\delta}$ is almost equal to $-\bar{H}_0$ and $\bar{P}$ is close to zero, as shown in Fig. 3(a), because the surface deformation and pressure can be neglected when the contact objects are distant. With the decrease of $\bar{H}_0$, the displacement $\bar{\delta}$ first increases before reaching a local maximum (denoted as point A), then decreases to a minimum (denoted as point B), and finally increases in a very steep way. If a displacement control method is adopted, there will be an unstable jumping-in position (A → A′) in the approaching process and an unstable jumping-out position (B → B′) in the detachment process, as illustrated in Fig. 3(b). For the surface central gap control method used, a full force–displacement curve is obtained, as shown in Fig. 3(b). It is found that the curve between the jumping-in and jumping-out positions is 'S-shaped'. The calculation path is along B′–A–B–A′–C–D, in which points A, B, C, and D represent the jumping-in, the jumping-out, the pull-off, and the zero-load points, respectively. For the displacement control method, the loading path is along B′–A–A′–C–D and the unloading path is along D–C–A′–B–B′. The area of the region B′–A–A′–B–B′ represents the dissipated mechanical energy, namely the hysteresis loss, which is caused by the unstable jumping during one loading/unloading cycle.

The corresponding JKR-n-k force–displacement curve (Chen et al., 2009b; Jin et al., 2021) is also plotted in Fig. 3(b). The FSCM and the JKR-n-k force–displacement curves coincide well along the high-load branch, but they are inconsistent along the low-load branch, which is due to the absence of surface interaction before jumping-in contact in the JKR-n-k model. It is found that the JKR-n-k model can well predict the jumping-out point (point B), but it cannot effectively predict the jump-in point (point A).

3.2. Effects of shape and material parameters

3.2.1. Effects of the shape index and the Tabor number

The effect of the Tabor number μ on the equilibrium force–displacement curve is analyzed for $n = 1$, 1.5, 2 and 5, as shown in Fig. 4. The representative value of k is chosen as 0.4. It can be seen that the adhesion hysteresis does not appear for a very small value of μ, and begins to appear and becomes notable with the increase of μ. For the cases of $n = 1$ and 1.5, the maximum value of $-\bar{P}$, i.e., the dimensionless pull-off force $-\bar{P}_c$, increases as μ increases, and the displacement at the pull-off point increases from a value close to 0 (corresponding to the Bradley pull-off point). For the cases of $n = 2$ and 5, the pull-off force decreases with the increase of μ, and the displacement at the pull-off point also decreases.

The effects of the Tabor number on the surface deformation and pressure distribution corresponding to the pull-off point are studied for $n = 2$ and $k = 0.4$. For all the Tabor numbers considered, the surface deformation at the pull-off point piles up in the edge zone of contact and approaches zero in the outer zone, as shown in Fig. 5(a). With the increase of $\bar{r}$, the pressure distribution at the pull-off point changes from compressive to tensile, and has a minimum near the edge of contact, as shown in Fig. 5(b). This minimum is known as the theoretical strength $-\sigma_{th}$ for a specific surface interaction law, which can be calculated from Eq. (10) as $\sigma_{th} \doteq 1.026\Delta\gamma/z_0$. With the increase of μ, the pile-up of surface is very massive and the corresponding pressure distribution near the theoretical strength becomes sharper. When μ is large (say ≥ 1), the surface deformation of the contact zone fits well with the punch profile (dash lines in Fig. 5(a)), which means that the gap $H(r)$ between the punch and the half-space is almost zero. Therefore, the so-called contact radius (an important parameter in the classical contact models such as the JKR-type and M–D-type models) can be easily defined under a large value of μ, e.g., the position corresponding to the theoretical strength $-\sigma_{th}$. However, for a small value
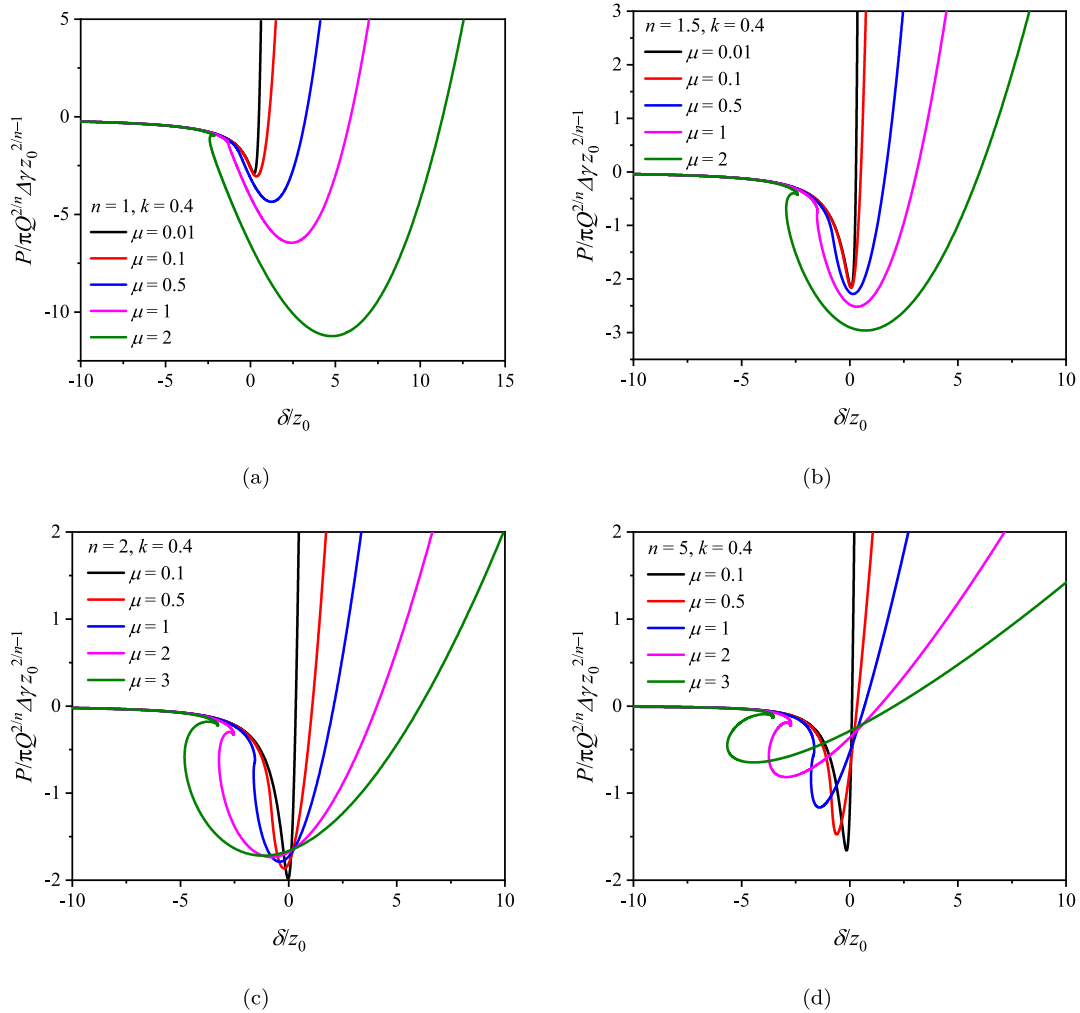
Fig. 4. The force–displacement curves for some special values of μ with $k = 0.4$ and different shape indexes: (a) $n = 1$, (b) $n = 1.5$, (c) $n = 2$, and (d) $n = 5$.

of μ (say 0.1), the surface deformation of the inner zone is very small and does not fit well with the punch profile, which means that the gap $H(r)$ is not close to zero in the inner zone. Therefore, the contact area in this case cannot be strictly defined, which indicates that the adhesive contact models using the contact radius as a parameter may be invalid for small Tabor numbers.

3.2.2. Effect of the gradient exponent

For fixed values of n and μ, the effect of k on the adhesion results is analyzed in this section. But, it should be noted that the Tabor number μ is related to the gradient exponent k in Eq. (29). A rigorous analysis of the effect of the gradient exponent should take the governing equations before dimensionless, which contains a large number of parameters. The comprehensive analysis becomes intractable due to the plethora of parameters associated with this issue. In fact, in practical problems, just changing the value of k is not trivial, because when producing graded materials, it is difficult to guarantee that E_0 at depth c_0 is identical. Therefore, the strategy of fixing n and μ and changing k is adopted here to get some understanding of the effect of the gradient exponent.

The dependency of the force–displacement curves on the gradient exponent k is studied for $n = 2$ and $\mu = 0.5$ and 1, as shown in Fig. 6. For the cases considered, the pull-off force increases monotonously with the increase of k, indicating that graded materials may have better adhesion properties compared with homogeneous materials. It can be concluded from Fig. 6 that the Tabor number rather than the gradient exponent determines whether the adhesion hysteresis occurs, but the gradient exponent may affect the jumping-in/out positions as long as the hysteresis exists.

The effects of k on the surface deformation and the pressure distribution corresponding to the pull-off point are studied for $n = 2$ and $\mu = 1$, as shown in Fig. 7. With the increase of k, the pile-up of surface becomes sharper and the pressure distribution also becomes sharper near the position corresponding to theoretical strength. In addition, the surface deformation and compressive pressure at the central point ($r = 0$) decrease as the gradient exponent increases.
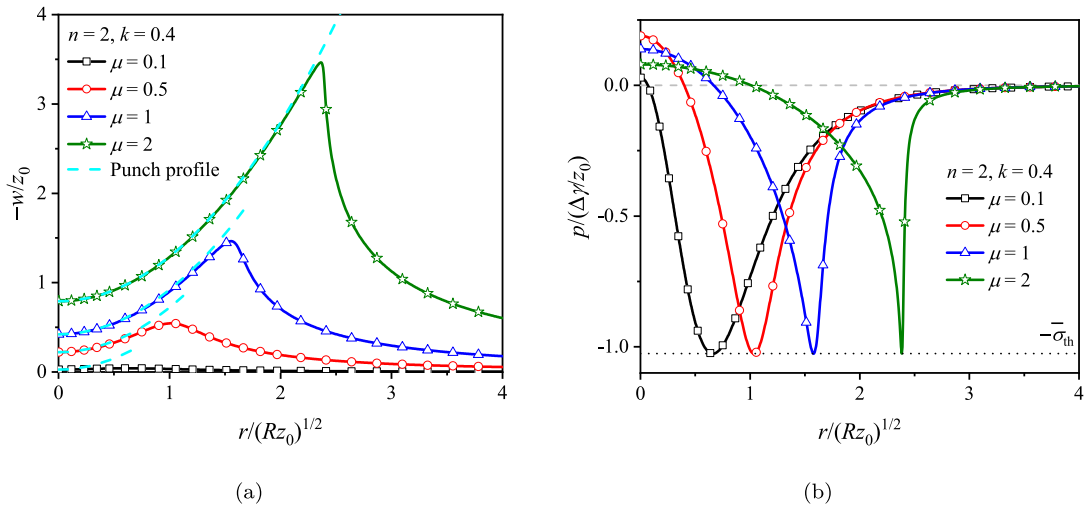
Fig. 5. Effects of the Tabor number on (a) the surface deformation and (b) pressure distribution at the pull-off point with $n = 2$ and $k = 0.4$.
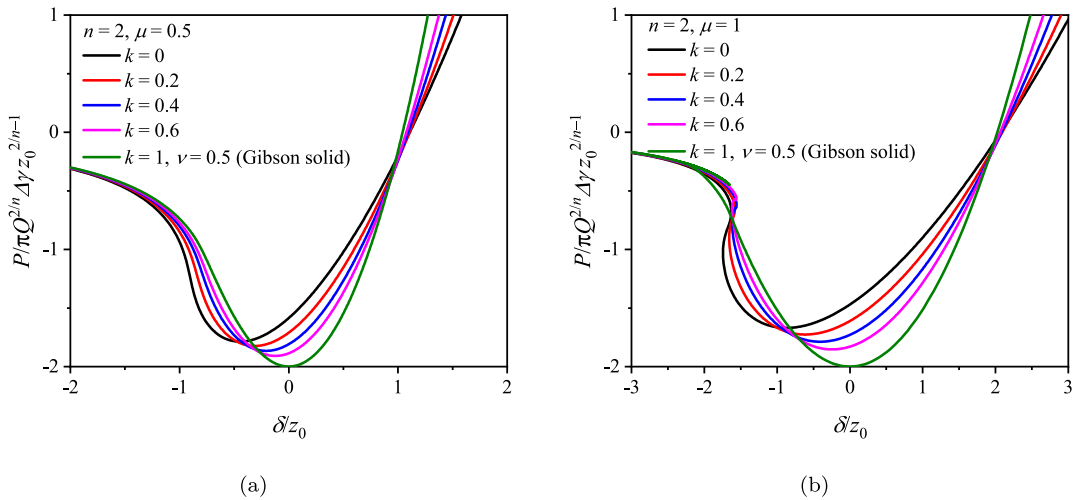

Fig. 6. The force–displacement curves for some special values of k: (a) $n = 2, \mu = 0.5$ and (b) $n = 2, \mu = 1$.
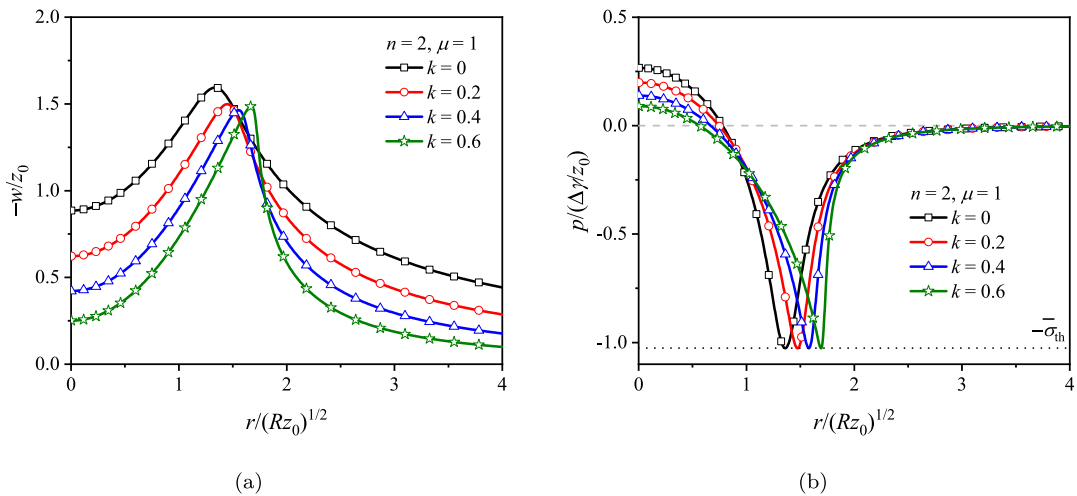

Fig. 7. Effect of the gradient exponent k on (a) the surface deformation and (b) pressure distribution at the pull-off point with $n = 2$ and $\mu = 1$.
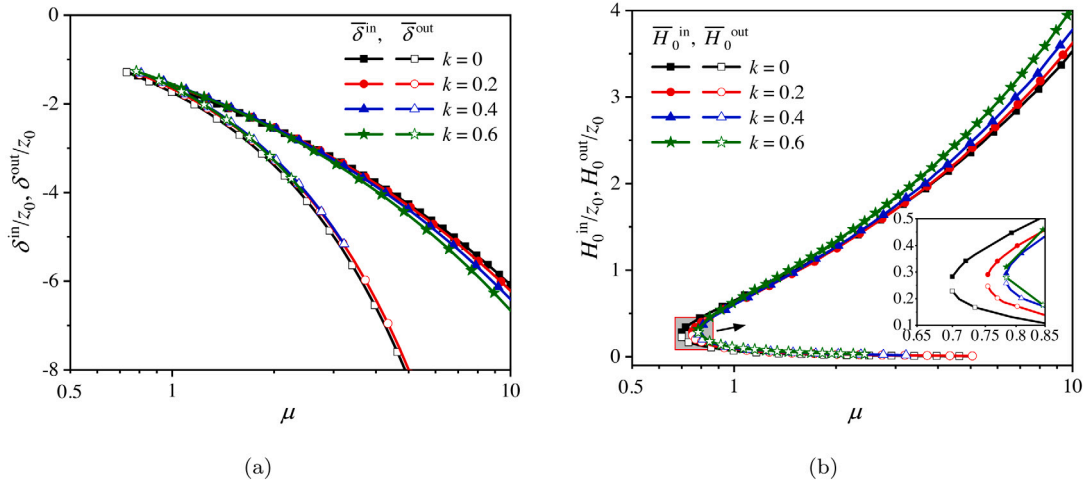
Fig. 8. Effect of the Tabor number on the (a) displacement and (b) surface central gap at the jumping-in/out points for four cases of $k = 0, 0.2, 0.4$ and 0.6 with $n = 2$.

3.3. The jumping-in/out instabilities

The adhesive hysteresis occurs under large Tabor numbers and may cause an energy hysteresis loss during one loading/unloading cycle, as discussed above. The positions of the jumping-in/out points (denoted as A/B) are paramount for calculating the hysteresis loss. Fig. 8 shows the effect of the Tabor numbers on the displacements ($\bar{\delta}^{in}, \bar{\delta}^{out}$) and surface central gaps ($\bar{H}_0^{in}, \bar{H}_0^{out}$) corresponding to the jumping-in/out points for four special values of gradient exponent k and $n = 2$. As can be seen from Fig. 8(a), with the increase of μ, the displacements (absolute value) at the jumping-in/out points increase monotonously, and the difference between the two displacements ($\left|\bar{\delta}^{in} - \bar{\delta}^{out}\right|$) also increases, indicating that the hysteresis phenomenon becomes more notable for the larger μ under fixed values of n and k. As μ increases, the surface central gap at the jumping-in point ($\bar{H}_0^{in}$) increases, and that at the jumping-out point ($\bar{H}_0^{out}$) decreases monotonously, as shown in Fig. 8(b). For given values of n and k, the two curves ($\bar{H}_0^{in}$ vs. μ and $\bar{H}_0^{out}$ vs. μ) intersect at a small value of μ, which is the critical Tabor number of the adhesion hysteresis phenomenon. The hysteresis only occurs when μ is larger than the critical value. In the four studied cases of $k = 0, 0.2, 0.4$ and 0.6, the critical Tabor numbers are about 0.70, 0.75, 0.78 and 0.78, respectively.

Although the numerical results of the jumping-in/out positions can be obtained from the FSCM, formula solutions are more convenient for practical application. Based on the FSCM, we extended the 'semi-rigid' theory for homogeneous materials (Greenwood, 2009; Song and Komvopoulos, 2014; Ciavarella et al., 2017) to that for power-law graded solids to obtain an explicit solution of the jumping-in displacement, as presented below. Near the jumping-in point, the surface central gap $\bar{H}_0$ is large (as shown in Fig. 8(b)), and it can be found from Eq. (27) that the surface traction $\bar{p}(\bar{r})$ is small, resulting in extremely small surface deformation $\bar{w}(\bar{r})$. Consequently, the material is assumed to be rigid in the 'semi-rigid' theory, in which the gap between the punch and the half-space is given by

$$\bar{H}(\bar{r}) \sim \bar{H}_0 + \bar{r}^n/n. \tag{40}$$

By combining this assumption with Eqs. (27), (31) and (33), the dimensionless displacement and load near the jumping-in point are calculated as

$$\bar{\delta} \sim -\bar{H}_0 + \frac{16n(1-k)(\mu/n)^{(2n+k-1)/n}}{3(\bar{H}_0+1)^{9-(1-k)/n}} \left[B\left(9 - \frac{1-k}{n}, \frac{1-k}{n}\right) - (\bar{H}_0+1)^6 B\left(3 - \frac{1-k}{n}, \frac{1-k}{n}\right) \right], \tag{41}$$

$$\bar{P} \sim \frac{16n^{(2-n)/n}}{3(\bar{H}_0+1)^{9-2/n}} \left[B\left(9 - \frac{2}{n}, \frac{2}{n}\right) - (\bar{H}_0+1)^6 B\left(3 - \frac{2}{n}, \frac{2}{n}\right) \right]. \tag{42}$$

Since only the low-load branch of the force–displacement curves up to the jumping-in point A is concerned here, the repulsive force (the ninth power term in Eq. (27)) is much smaller than the attractive force (the third power term in Eq. (27)). As a result, the first term in the bracket of Eqs. (41) and (42) is much smaller than the second one, and can be neglected in the following mathematical derivation. A similar approximation has been proposed in the literature (Wu, 2010; Ciavarella et al., 2017) for the contact problems between a sphere and homogeneous materials. By applying this approximation, Eqs. (41) and (42) can be rewritten as

$$\bar{\delta} \sim -\bar{H}_0 - \frac{16(1-k)\mu^{2-(1-k)/n}}{3n^{1-(1-k)/n}(\bar{H}_0+1)^{3-(1-k)/n}} B\left(3 - \frac{1-k}{n}, \frac{1-k}{n}\right), \tag{43}$$

$$\bar{P} \sim -\frac{16n^{(2-n)/n}}{3(\bar{H}_0+1)^{3-2/n}} B\left(3 - \frac{2}{n}, \frac{2}{n}\right). \tag{44}$$
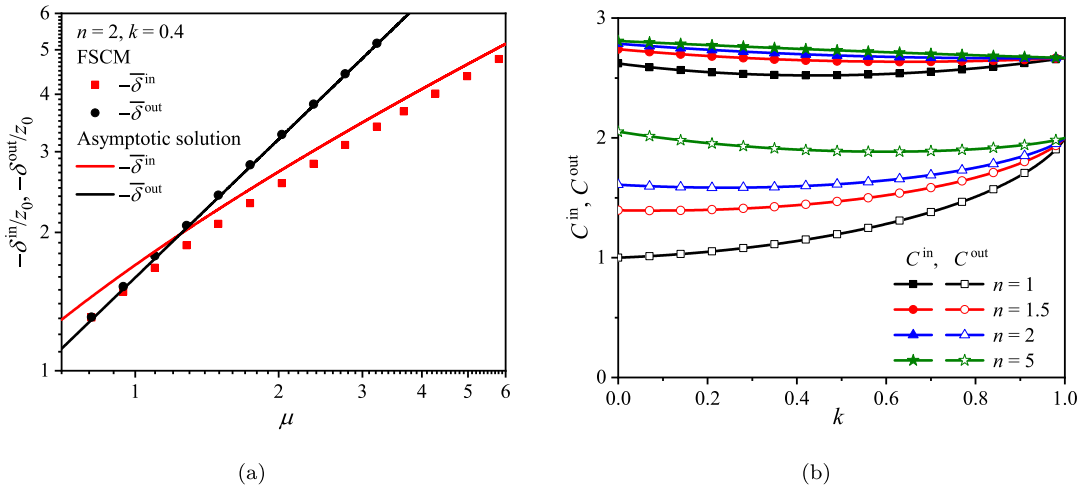
Fig. 9. (a) Comparison of the jumping displacements between the FSCM and the asymptotic solutions as the Tabor number varies; (b) Effect of k on C^{in} and C^{out} for different n.

The jumping-in condition is given by

$$\left(\frac{\mathrm{d}\bar{\delta}}{\mathrm{d}\bar{P}}\right)_{\text{A}} = \left(\frac{\mathrm{d}\bar{\delta}/\mathrm{d}\bar{H}_0}{\mathrm{d}\bar{P}/\mathrm{d}\bar{H}_0}\right)_{\text{A}} = 0, \tag{45}$$

where subscript A represents the jumping-in point. Note that $\mathrm{d}\bar{P}/\mathrm{d}\bar{H}_0$ in Eq. (45) always has a finite value, thus one has $\left(\mathrm{d}\bar{\delta}/\mathrm{d}\bar{H}_0\right)_{\text{A}} = 0$. By combining this condition with Eq. (43), the surface central gap at the jumping-in point A can be derived as

$$\bar{H}_0^{\text{in}} = \left[\frac{16(1-k)(3n+k-1)}{3n^{(2n+k-1)/n}}\mathrm{B}(3 - \frac{1-k}{n}, \frac{1-k}{n})\mu^{(2n+k-1)/n}\right]^{n/(4n+k-1)} - 1. \tag{46}$$

Substituting Eq. (46) into Eq. (43) leads to the displacement at the jumping-in point

$$\bar{\delta}^{\text{in}} = 1 - C^{\text{in}}\mu^{(2n+k-1)/(4n+k-1)}, \tag{47}$$

where C^{in} is given by

$$C^{\text{in}} = \frac{4n+k-1}{3n+k-1}\left[\frac{16(1-k)(3n+k-1)}{3n^{(2n+k-1)/n}}\mathrm{B}(3 - \frac{1-k}{n}, \frac{1-k}{n})\right]^{n/(4n+k-1)}. \tag{48}$$

This asymptotic solution (Eq. (47)) coincides well with the FSCM results, as shown in Fig. 9(a) for $n = 2$ and $k = 0.4$. Eq. (47) indicates that the dimensionless jumping-in displacement $\bar{\delta}^{\text{in}}$ is positively correlated with $\mu^{(2n+k-1)/(4n+k-1)}$. For $n = 2$ and $k = 0$, Eq. (47) reduces to the asymptotic solution in the special case of a rigid sphere in contact with homogeneous elastic materials (Ciavarella et al., 2017), given by

$$\bar{\delta}^{\text{in}} = 1 - \frac{7}{5}\left(\frac{5\pi}{\sqrt{2}}\right)^{2/7}\mu^{3/7}. \tag{49}$$

However, the 'semi-rigid' theory cannot be applied to predict the positions of the jumping-out points, because the surface central gap is small (as shown in Fig. 8(b)) and the surface deformation cannot be neglected. Note that for small Tabor numbers, the jumping instabilities do not appear, while for large Tabor numbers, the JKR-n-k model coincides well with the FSCM at the high-load branch, as discussed above. Actually, the asymptotic solution of the jumping-out position can be derived from the JKR-n-k theory, as given below. The displacement and force of the JKR-n-k model are given by (Jin et al., 2021)

$$\delta = \frac{1}{2Q}\mathrm{B}(\frac{n}{2}, \frac{1+k}{2})a^n - \left(\frac{2\pi bc_0^k\Delta\gamma}{\cos(k\pi/2)E^*}\right)^{1/2}a^{(1-k)/2}, \tag{50}$$

$$P = \frac{\cos(k\pi/2)E^*}{b(1+k)Qc_0^k}\mathrm{B}(1 + \frac{n}{2}, \frac{1+k}{2})a^{n+k+1} - \left[\frac{8\pi\cos(k\pi/2)\Delta\gamma E^*}{b(1+k)^2c_0^k}\right]^{1/2}a^{(3+k)/2}. \tag{51}$$

where parameter a is the contact radius. The jumping-out condition is given by

$$\left(\frac{\mathrm{d}\delta}{\mathrm{d}P}\right)_{\text{B}} = \left(\frac{\mathrm{d}\delta/\mathrm{d}a}{\mathrm{d}P/\mathrm{d}a}\right)_{\text{B}} = 0, \tag{52}$$

where subscript B represents the jumping-out point. Note that dP/da in Eq. (52) always has a finite value, thus one has $(d\delta/da)_B = 0$. By combining this condition with Eq. (50), the contact radius at the jumping-out point B can be derived as

$$a^{\text{out}} = \left[\frac{2\pi bc_0^k \Delta\gamma}{\cos(k\pi/2)E^*} \left(\frac{Q(1-k)}{n\text{B}(n/2, 1/2 + k/2)} \right)^2 \right]^{1/(2n+k-1)}. \tag{53}$$

Substituting Eq. (53) into Eq. (50) leads to

$$\bar{\delta}^{\text{out}} \equiv \frac{\delta^{\text{out}}}{z_0} = -C^{\text{out}}\mu, \tag{54}$$

where C^{out} is given by

$$C^{\text{out}} = \frac{1}{2}(2n+k-1)\left[\frac{2\pi(1-k)}{n^2\cos(k\pi/2)} \right]^{n/(2n+k-1)} \left(\frac{1-k}{\text{B}(n/2, 1/2+k/2)} \right)^{(1-k)/(2n+k-1)}. \tag{55}$$

Eq. (54) indicates that the dimensionless jumping-out displacement is proportional to the Tabor number μ. The asymptotic solution Eq. (54) agrees well with the FSCM results, as shown in Fig. 9(a) for $n = 2$ and $k = 0.4$.

So far, we have derived two asymptotic solutions concerning the positions of the jumping-in point and the jumping-out point, given by Eqs. (47) and (54), respectively. The dependency of the coefficients C^{in} and C^{out} on the gradient index k is shown in Fig. 9(b) for $n = 1, 1.5, 2$ and 5. For a given value of $0 \le k < 1$, both C^{in} and C^{out} increase with the increase of n. As $k \to 1$, C^{in} approaches to $8/3$ and C^{out} approaches to 2, and these limit values are independent of the shape index n.

3.4. The JKR–Bradley transition for power-law graded materials

The effect of the Tabor number μ on the pull-off force is studied for $k = 0, 0.2, 0.4$ and 0.6 and four representative values of n, as shown in Fig. 10. The dimensionless pull-off force approaches a constant value for small μ, namely the Bradley-n limit. The normalized Bradley-n pull-off force has been given by (Zheng and Yu, 2007b)

$$-\bar{P}_c^{\text{Bradley-}n} = \frac{32n^{2/n}}{9n-2}\text{B}(3-\frac{2}{n}, \frac{2}{n})\left(168\text{B}(4-\frac{2}{n}, 6) \right)^{(3-2/n)/6}, \tag{56}$$

which gives the values of $2.880, 2.166, 2$ and 1.669 for $n = 1, 1.5, 2$ and 5, respectively. The dimensionless Bradley-n pull-off force is independent of k because it represents the rigid limit. At the large-μ extreme, the dependence of the dimensionless pull-off force on μ is positive for $n < 2$ and negative for $n > 2$. This understanding is different from that of Jin et al. (2021) because different dimensionless methods are used. This issue will be further discussed in Section 4. When μ is very large, the FSCM curve asymptotically approaches a straight line for each n in the log–log scale coordinates system, which is the corresponding JKR-n-k solution. From Eq. (51), the normalized JKR-n-k pull-off force is given by (Jin et al., 2021)

$$-\bar{P}_c^{\text{JKR-}n\text{-}k} = \frac{2(2n+k-1)}{(1+k)(n+k+1)}\left[\left(\frac{\cos(k\pi/2)}{2\pi(1-k)} \right)^{n-2} \left(\frac{k+3}{n\text{B}(n/2, 1/2+k/2)} \right)^{k+3} \right]^{1/(2n+k-1)} \mu^{(2-n)/n}. \tag{57}$$

As the Tabor number μ changes from zero to infinity, a continuous transition from the Bradley-n model to the JKR-n-k model is obtained by the FSCM for the power-law graded materials.

For given Tabor numbers with $n = 1.5$ and 2, the dimensionless pull-off force of the graded material increases with the increase of k and is larger than that of the homogeneous material over the whole transition (except for the rigid limit), as shown in Figs. 10(b) and 10(c). In addition, the JKR–Bradley transition curve approaches the JKR-n-k limit at smaller Tabor numbers as k increases for $n = 1.5$ and 2. But for $n = 1$ and 5, the pull-off force is not sensitive to the value of k, as shown in Figs. 10(a) and 10(d). To quantify the sensitivity of the pull-off force to k, the relative deviation of the pull-off force between the graded and homogeneous materials predicted by the JKR-type models (Jin et al., 2021; Zheng and Yu, 2007b) is calculated, which is

$$\chi = \left| \frac{\bar{P}_c^{\text{JKR-}n\text{-}k} - \bar{P}_c^{\text{JKR-}n}}{\bar{P}_c^{\text{JKR-}n}} \right|. \tag{58}$$

The effect of k on the value of χ is explored in Fig. 11(a). The maximum of χ is $4.4\%, 40.8\%, 33.3\%$ and 4.2% for $n = 1, 1.5, 2$ and 5, respectively, which indicates that, for given Tabor numbers, k has a large effect on the pull-off force with $n = 1.5$ and 2, and a small effect with $n = 1$ and 5. Fig. 11(b) plots the variation of the maximum relative deviation with n. It can be found that the maximum of the relative deviation χ_{max} is particularly small in two regions. If the relative deviation is limited to 10%, the two regions are $0.974 \le n \le 1.056$ and $3.335 \le n \le 6.219$. But, this does not mean that k has no effect in the two regions because the Tabor number (Eq. (29)) is related to k. It can be concluded that the dimensionless pull-off force usually depends on the three dimensionless parameters (n, μ and k), but when n is near 1 or in the range of $(3.3, 6.2)$, the dimensionless pull-off force mainly depends on n and μ.
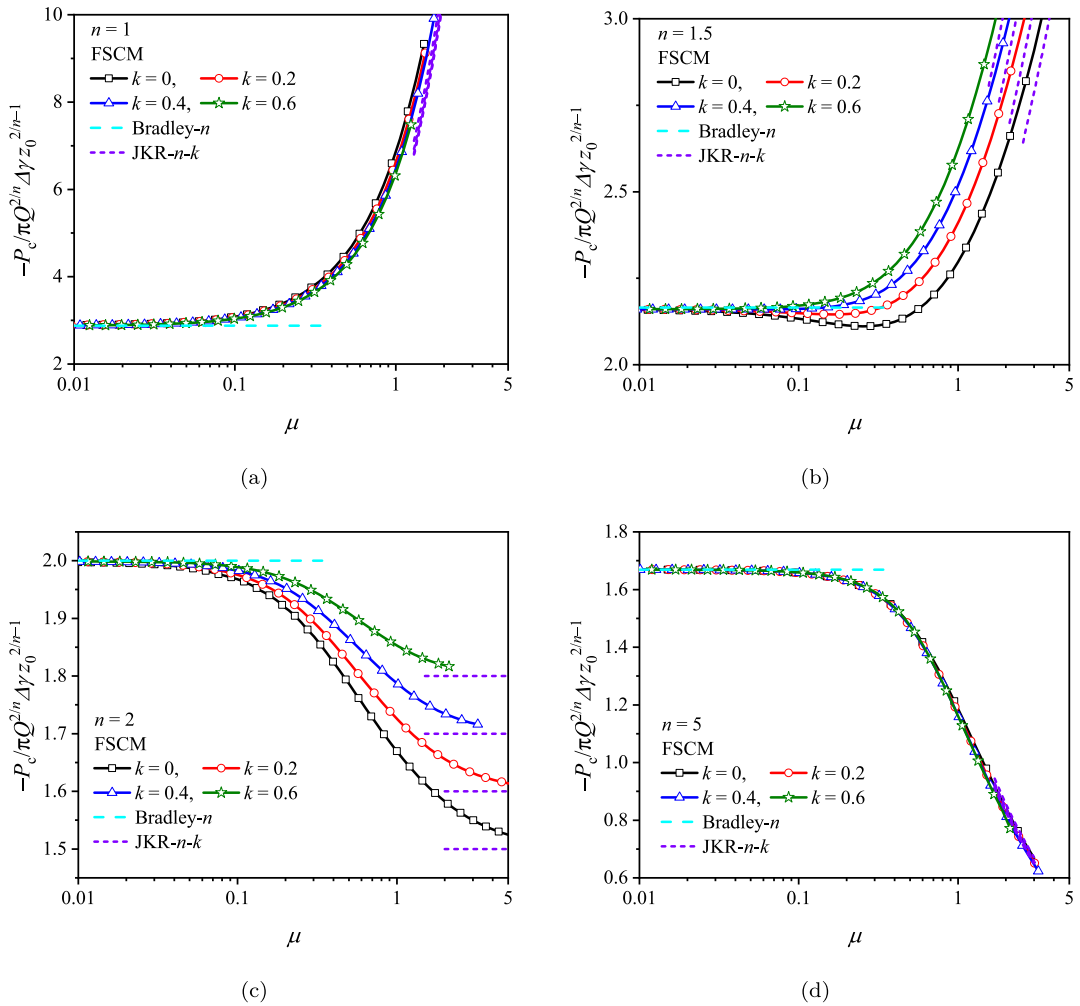
Fig. 10. Variation of the dimensionless FSCM pull-off force with the Tabor number for four special values of k with (a) $n = 1$, (b) $n = 1.5$, (c) $n = 2$, and (d) $n = 5$. The Bradley-n limits (dash line) and the JKR-n-k limits (short dash line) are also plotted.
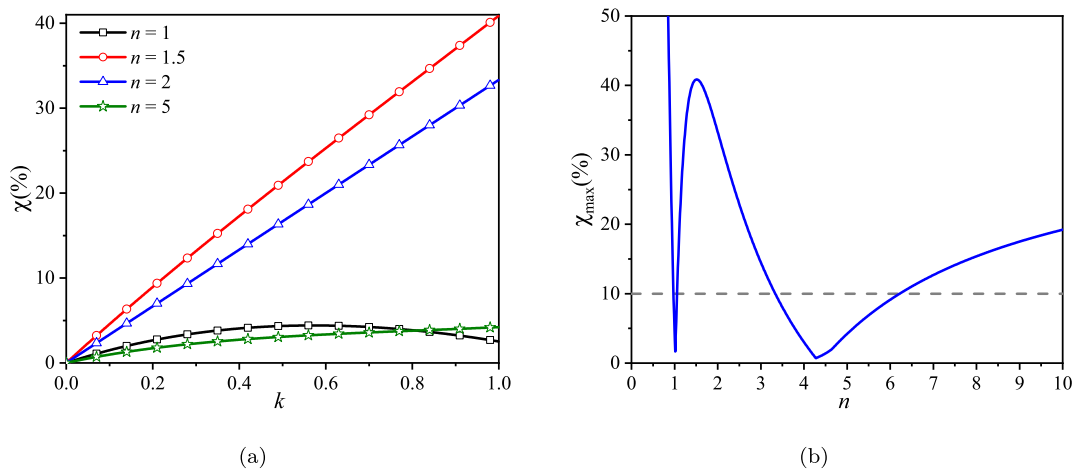

Fig. 11. (a) Effect of k on the relative deviation of the pull-off force predicted by the JKR-n-k model between the graded and homogeneous materials. (b) Maximum relative deviation as a function of n.

4. Application to verify the M–D-*n-k* model

4.1. Overview of the M–D-n-k model

It is worth emphasizing the basic relations of the Maugis–Dugdale (M–D) model (Maugis, 1992). The first relation is the Hertzian assumption of the close contact condition

$$H(r) = 0, \quad r < a. \tag{59}$$

The second one is the stress non-singularity condition at the contact edge ($r = a$)

$$\lim_{r \to a} \sqrt{2\pi (a - r)} p_s(H(r)) = 0. \tag{60}$$

The last relation is taken from the fracture mechanics principle, namely the Griffith relation over the cohesive zone ($a < r < c$)

$$-\int_{r=a}^{r=c} p_s(H(r)) dH(r) = \Delta\gamma. \tag{61}$$

The Dugdale approximation is usually adopted to give the stress in the cohesive zone,

$$p_s(H(r)) = -\sigma_0, \quad a < r < c, \tag{62}$$

where σ_0 is a constant value, namely the cohesive stress.

The M–D model has been extended for different surface shapes or materials in the literature (Goryacheva and Makhovskaya, 2001; Zheng and Yu, 2007a,b; Johnson and Greenwood, 2008; Wu, 2009; Grierson et al., 2013; Jin et al., 2018). Recently, the M–D model was extended to the power-law graded materials (M–D-*n-k* model) based on the principle of superposition (Jin et al., 2021). By introducing the following dimensionless variables

$$\tilde{\delta} \equiv \delta / \left[c_0^{nk} Q^{1-k} \Delta\gamma^n E^{*-n} b^n (1-k)^{-n} \right]^{1/(2n+k-1)}, \tag{63}$$

$$\tilde{P} \equiv P / \left[\pi \left(c_0^{(2-n)k} Q^{3+k} \Delta\gamma^{n+k+1} E^{*n-2} b^{2-n} (1-k)^{n-2} \right)^{1/(2n+k-1)} \right], \tag{64}$$

$$\tilde{a} \equiv a / \left[c_0^k Q^2 \Delta\gamma E^{*-1} b (1-k)^{-1} \right]^{1/(2n+k-1)}, \tag{65}$$

the M–D-*n-k* results (Jin et al., 2021) can be rewritten in a dimensionless form as

$$\tilde{\delta} = \frac{\tilde{a}^n}{2} B(\frac{n}{2}, \frac{1+k}{2}) - 2\Lambda \tilde{a}^{1-k} (m^2 - 1)^{(1-k)/2}, \tag{66}$$

$$\tilde{P} = \frac{\tilde{a}^{n+k+1}}{\pi (1-k^2)} \cos \frac{k\pi}{2} B(1 + \frac{n}{2}, \frac{1+k}{2}) - \Lambda (m^2 - \omega_1 m^{1-k}) \tilde{a}^2, \tag{67}$$

where Λ is the generalized Maugis number, defined as

$$\Lambda = \sigma_0 \left[\frac{Q^{1-k} c_0^{nk} \Delta\gamma^{1-n-k} b^n}{E^{*n} (1-k)^n} \right]^{1/(2n+k-1)}, \tag{68}$$

and parameter $m = c/a$ is derived from the Griffith relation

$$\Lambda^2 \tilde{a}^{1-k} \left[2 (m^2 - 1)^{(1-k)/2} - \frac{\Gamma(2-k) m^{1-k}}{(\Gamma(3/2 - k/2))^2} + \frac{\omega_2}{m^{2k}} \right] + \Lambda \tilde{a}^n \left[\frac{m^n}{n} + \frac{1}{2} \left(\frac{\omega_3}{m^{1+k}} - 1 \right) B(\frac{n}{2}, \frac{1+k}{2}) \right] = 1, \tag{69}$$

where $\Gamma(\cdot)$ is the Gamma function. In the above equations, ω_1, ω_2 and ω_3 are defined as

$$\omega_1 = \frac{4 \cos(k\pi/2)}{\pi (1-k^2)} \left[{}_2F_1(\frac{k-1}{2}, \frac{k+1}{2}; \frac{k+3}{2}; \frac{1}{m^2}) - m^{k-1} (m^2 - 1)^{(1-k)/2} \right], \tag{70}$$

$$\omega_2 = \frac{4 \cos(k\pi/2)}{\pi (1+k)} \left[{}_2F_1(k, \frac{k+1}{2}; \frac{k+3}{2}; \frac{1}{m^2}) - m^{k-1} (m^2 - 1)^{(1-k)/2} {}_2F_1(\frac{k+1}{2}, \frac{k+1}{2}; \frac{k+3}{2}; \frac{1}{m^2}) \right], \tag{71}$$

$$\omega_3 = \frac{2 \cos(k\pi/2)}{\pi (1+k)} \left[{}_2F_1(\frac{k+1}{2}, \frac{k+1}{2}; \frac{k+3}{2}; \frac{1}{m^2}) - \frac{k+1}{n+k+1} {}_2F_1(\frac{k+1}{2}, \frac{n+k+1}{2}; \frac{n+k+3}{2}; \frac{1}{m^2}) \right]. \tag{72}$$

It should be pointed out that the definitions of the dimensionless variables in Eqs. (63)–(65) and the generalized Maugis number Λ defined by Eq. (68) are slightly different from those in Jin et al. (2021) because parameter b is included in the present dimensionless parameters. Similar to the Tabor number, defining the generalized Maugis number in the present way can reduce one dimensionless parameter from the similarity model. Consequently, for the M–D-*n-k* model, the similarity model only contains three dimensionless parameters, namely the shape index n, the gradient exponent k, and the generalized Maugis number Λ. Eqs. (66)–(72) can be reduced to the homogeneous case ($k = 0$) (Zheng and Yu, 2007a,b), and further to the classical case of $n = 2$ and $k = 0$ (Maugis, 1992). An additional condition is required to determine the value of the cohesive stress σ_0, which will be discussed in detail in the following section.

4.2. Two strategies to determine the cohesive stress

The value of the cohesive stress σ_0 has a great effect on the M–D-type results, but it may not be selected correctly in the extensive literature. In the classical M–D model ($n = 2$, $k = 0$), Maugis (1992) chose σ_0 equal to the theoretical stress of the L–J law, written as

$$\sigma_0 = \sigma_{\text{th}} = \frac{16\sqrt{3}\Delta\gamma}{27z_0} \doteq 1.026\frac{\Delta\gamma}{z_0}, \tag{73}$$

which relates Λ and μ by $\Lambda \doteq 1.026\mu$. This strategy can be referred to as *the maximum strength condition*, which seems to have some physical meanings, because the cohesive stress cannot exceed the theoretical stress at least. But, there is no evidence that this value is appropriate. Even so, this traditional strategy was adopted by almost all the later researchers when they extended the M–D model to different surface shapes or materials (Goryacheva and Makhovskaya, 2001; Johnson and Greenwood, 2008; Wu, 2009; Grierson et al., 2013; Jin et al., 2018). Jin et al. (2021) also adopted *the maximum strength condition* when developing the M–D-*n-k* model, but ignored the decimal part of 1.026, which results in $\sigma_0 = \Delta\gamma/z_0$ and $\Lambda = \mu$. So, Jin et al. (2021) did not distinguish the generalized Tabor and Maugis numbers in their M–D-*n-k* model.

Greenwood (1997) pointed out that there was no exact correspondence between the Maugis number and the Tabor number since a simplified surface force curve (the Dugdale law) is assumed in the M–D model. Johnson and Greenwood (1997) emphasized that the strategy that σ_0 was chosen to be the maximum L–J tension is somewhat arbitrary, but they did not give a better value. Jin et al. (2021) observed that there is an apparent difference between the finite element results and the M–D-*n-k* model using *the maximum strength condition*, which was attributed to the sensitivity of the surface interaction form, but they did not suggest an appropriate strategy to determine the interaction either. Johnson and Greenwood (1997) pointed out that the Maugis model based on the Dugdale approximation is rough and the deviation can be evaluated by comparing it with the FSCM based on the L–J law. Therefore, an appropriate strategy for choosing the value of σ_0 is to keep the deviation between the M–D-type model and the FSCM as small as possible. To realize this goal, the cohesive stress σ_0 may depend on the surface shape parameters (e.g., n) and the material parameters (e.g., k), and could change during the whole contact/detachment process, which makes the M–D-type model lose its conciseness.

In response to this difficulty, Zheng and Yu (2007b) proposed an alternative strategy to determine the value of σ_0 when developing the M–D-*n* model for homogeneous materials ($k = 0$) with power-law surface shape, which is described as follows. As Λ and μ approach zero, the M–D-*n* model and the FSCM reduce to the DMT-*n* model and the Bradley-*n* model, respectively. Notice that the pull-off point of the DMT-*n* model occurs at zero contact radius ($a = 0$), where there is no deformation. So, the DMT-*n* model should be identical with the rigid model (i.e., the Bradley-*n* model) at the pull-off point. In the Zheng and Yu's strategy, σ_0 is chosen to make the DMT-*n* pull-off force identical to the Bradley-*n* pull-off force, i.e.

$$- P_{\text{c}}^{\text{DMT-}n} = - P_{\text{c}}^{\text{Bradley-}n}, \tag{74}$$

which can be named as *the rigid-limit-consistency condition*. The value of σ_0 using this condition depends only on the surface shape parameter n through a specific function, which maintains the conciseness of the M–D model. In addition, the improved M–D model using this condition shows much better consistency with the FSCM, compared with the original M–D model using *the maximum strength condition*, as shown in Figs. 5–7 of Zheng and Yu (2007b).

Therefore, in the present study, we apply *the rigid-limit-consistency condition* to improve the M–D-*n-k* model. For power-law graded materials, the Bradley pull-off force is given by Eq. (56) and the DMT pull-off force is (Jin et al., 2021)

$$- P_{\text{c}}^{\text{DMT-}n\text{-}k} = \pi(nQ\Delta\gamma)^{2/n}\sigma_0^{1-2/n}, \tag{75}$$

which is independent of the gradient exponent k. In fact, for any kind of graded materials, the pull-off forces of the Bradley and DMT models are both independent of the elastic parameters such as the reference modulus and the gradient exponent. It can be expected that *the rigid-limit-consistency condition* for graded materials is the same as the one (Eq. (74)) for homogeneous materials. Substituting Eqs. (56) and (75) into Eq. (74) yields

$$\sigma_0 = \eta(n)\frac{\Delta\gamma}{z_0}, \tag{76}$$

where $\eta(n)$ is defined as (Zheng and Yu, 2007b)

$$\eta(n) = \left[\frac{32}{9n-2}\text{B}\left(3 - \frac{2}{n}, \frac{2}{n}\right)\left(168\text{B}\left(4 - \frac{2}{n}, 6\right)\right)^{(3-2/n)/6}\right]^{n/(n-2)}. \tag{77}$$

Substituting Eqs. (29) and (68) into Eq. (76) leads to

$$\Lambda = \eta(n)\mu. \tag{78}$$

Consequently, the improved M–D-*n-k* model can be acquired by combining Eqs. (66)–(72) and Eq. (76). The value of σ_0 in the improved M–D-*n-k* model is an exclusive value, which is determined by the surface shape index n through the function $\eta(n)$. The function $\eta(n)$ increases monotonically with n, as plotted in Fig. 12(a) with a solid line. As $n \to \infty$, $\eta(n) \to 1.026$, which corresponds to the theoretical stress σ_{th} used in the original M–D-*n-k* model (Jin et al., 2021), as plotted in Fig. 12(a) with a dotted line. For the four special cases of $n = 1, 1.5, 2$ and 5 considered, the values of $\eta(n)$ are 0.347, 0.499, 0.588 and 0.803, respectively, as shown in Fig. 12(a).
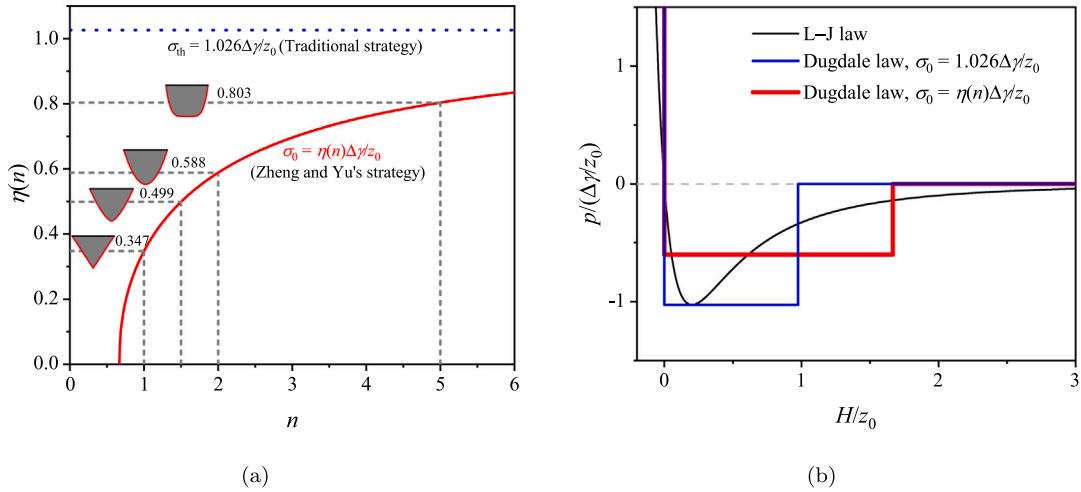
Fig. 12. (a) The function of $\eta(n)$ and the theoretical stress σ_{th}. (b) Variation of the surface pressure with the surface separation for the FSCM and the original and improved M–D-*n-k* models.

The variation of the surface pressure with the surface separation is shown in Fig. 12(b) for the FSCM, the original M–D-*n-k* model ($\sigma_0 = 1.026\Delta\gamma/z_0$), and the improved M–D-*n-k* model ($\sigma_0 = \eta(n)\Delta\gamma/z_0$). The integral areas of the three curves below the H-axis are $-\Delta\gamma$, which means that the strain energy release rate is equal to the surface energy, i.e., the Griffith relation is satisfied in the three models. The value of σ_0 in the improved M–D-*n-k* model is smaller than that in the original M–D-*n-k* model, so the width of the cohesive zone (i.e., $c - a$) of the former is larger than that of the latter to keep their areas identical.

4.3. Validations of the M–D-*n-k* model

4.3.1. The force–displacement curves

As the FSCM is the most accurate adhesive contact model in the continuum framework, we apply it to validate the M–D-*n-k* models with different selection strategies of cohesive stress σ_0. The force–displacement curves of the original and improved M–D-*n-k* models are compared with the corresponding FSCM results in Fig. 13 for four special values of n. Fixed parameters are $k = 0.4$ and $\mu = 1$. Compared with the original M–D-*n-k* model (Jin et al., 2021), the improved M–D-*n-k* model shows a better agreement with the FSCM results for the cases considered. For $n = 1$, 1.5 and 2 in Fig. 13, the improved M–D-*n-k* model almost coincides with the FSCM for the contact parts. For $n = 5$ in Fig. 13(d), the improved M–D-*n-k* model still shows superiority over the original one, despite the fact that the force of the improved M–D-*n-k* model is larger than that of the FSCM, which can be attributed to the oversimplification of the surface interaction in the cohesive zone of the M–D model itself. It can be concluded from Fig. 13 that *the rigid-limit-consistency condition* can significantly improve the accuracy of the M–D-*n-k* force–displacement curves when compared with the FSCM.

4.3.2. The pull-off force

The pull-off force as a function of Tabor number μ is studied for the cases of $k = 0.4$ and $n = 1$, 1.5, 2 and 5, as shown in Fig. 14. For the cases considered, the predictions of the original and improved M–D-*n-k* models agree well with the FSCM results for large μ (say 2), because the M–D-*n-k* models reduce to the JKR-*n-k* model at large μ, which is independent of the value of σ_0. For $n = 2$ in Fig. 14(c), the M–D-*n-k* models coincide well with the FSCM for very small and large μ (e.g., 0.01 and 2), but the improved M–D-*n-k* model shows a much better agreement than the original one over a wide range of moderate Tabor numbers (say 0.05–2). For $n \neq 2$ in Fig. 14, the results of the improved M–D-*n-k* model are very close to those of the FSCM, but a great discrepancy is observed between the original M–D-*n-k* model (Jin et al., 2021) and FSCM results for small and moderate Tabor numbers (e.g., $\mu < 2$).

The pull-off force is scaled by the magnitude of the rigid limit, thus it approaches constant values for small Tabor numbers, as shown in Fig. 15. It can be seen clearly from Fig. 15 that the improved M–D-*n-k* model shows a better agreement with the FSCM over the whole JKR–Bradley transition than the original one. If the pull-off force is scaled by the magnitude of the soft limit (Jin et al., 2021), it approaches constant values for large Tabor numbers, as shown in Fig. 16(a). The discrepancy in Fig. 16(a) seems not significant, because the range of the vertical axis is too large in this scaling way. Actually, the relative error κ of the pull-off force between the M–D-*n-k* models and the FSCM is identical in the two scaling ways, which can be used as a parameter to judge the accuracy of the M–D-*n-k* models. Fig. 16(b) plots the variation of the relative errors κ of the M–D-*n-k* models as a function of the Tabor number μ for $k = 0.4$ with four representative values of n. For all cases, the relative errors κ of the original and improved M–D-*n-k* models approach zero at large μ (say $\mu > 2$). For small and moderate Tabor numbers (say $\mu < 2$), the relative error of the improved M–D-*n-k* model (solid line) compared with the FSCM is much smaller than that of the original M–D-*n-k* model (dash line)
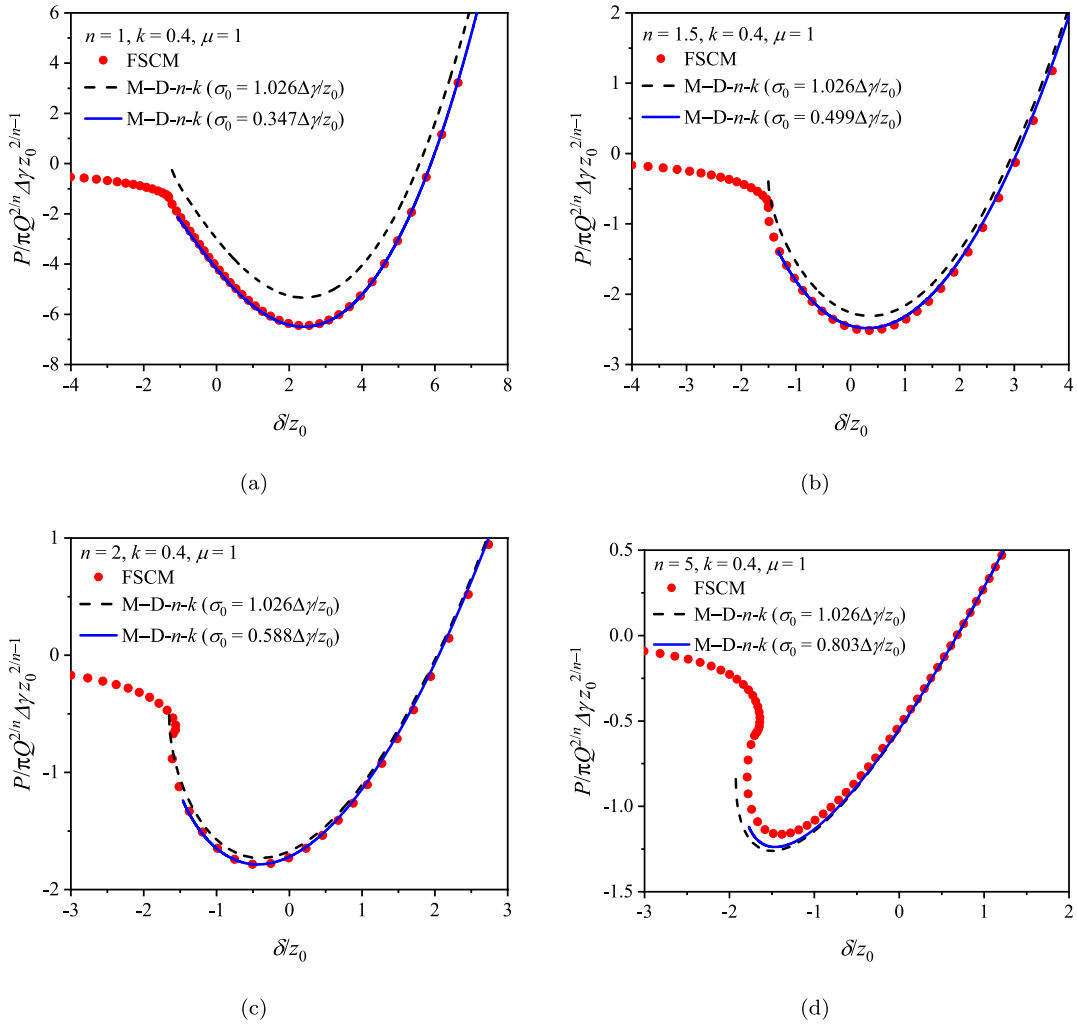
Fig. 13. Validating the force–displacement curves of the original and improved M–D-n-k models by comparing with the FSCM results for (a) $n = 1$, (b) $n = 1.5$, (c) $n = 2$ and (d) $n = 5$ with $k = 0.4$ and $\mu = 1$.

with $n = 1$, 1.5 and 5. For example, the maximum relative errors of the original M–D-n-k model (Jin et al., 2021) are 65.0%, 21.2% and 15.9% for $n = 1$, 1.5 and 5, respectively, whereas the corresponding values of the improved M–D-n-k model are only 5.8%, 1.7% and 6.7%. For $n = 2$, the relative errors of the original and improved M–D-n-k models are both close to zero for small and large μ. But for moderate μ in this case, the improved M–D-n-k model can still show its superiority over the original one, e.g., the maximum relative errors of the original and improved models are 3.5% and 0.73%, respectively. Therefore, it is concluded that *the rigid-limit-consistency condition* (Eq. (74)) can greatly improve the accuracy of the M–D-n-k pull-off forces over the whole JKR–Bradley transition when compared with the FSCM.

4.3.3. Surface deformation and pressure distribution

The surface deformation and pressure distribution of the M–D-n-k models with two selecting strategies of the cohesive stress corresponding to the pull-off point are shown in Fig. 17, where the FSCM results are also plotted for comparison. The surface deformation of the improved M–D-n-k model shows a slightly better agreement with that of the FSCM inside the contact zone ($r < a$) and outside the cohesive zone ($r > c$) when compared with the original one, as shown in Fig. 17(a). In the cohesive zone ($a < r < c$), the surface deformations of both the original and improved M–D-n-k models do not coincide with the FSCM results, because the surface pressure is over-simplified in this zone, as shown in Fig. 17(b). The surface deformation of the original model is sharp and that of the improved model is smooth, because the latter has a smaller value of σ_0 and a wider cohesive zone than the former.
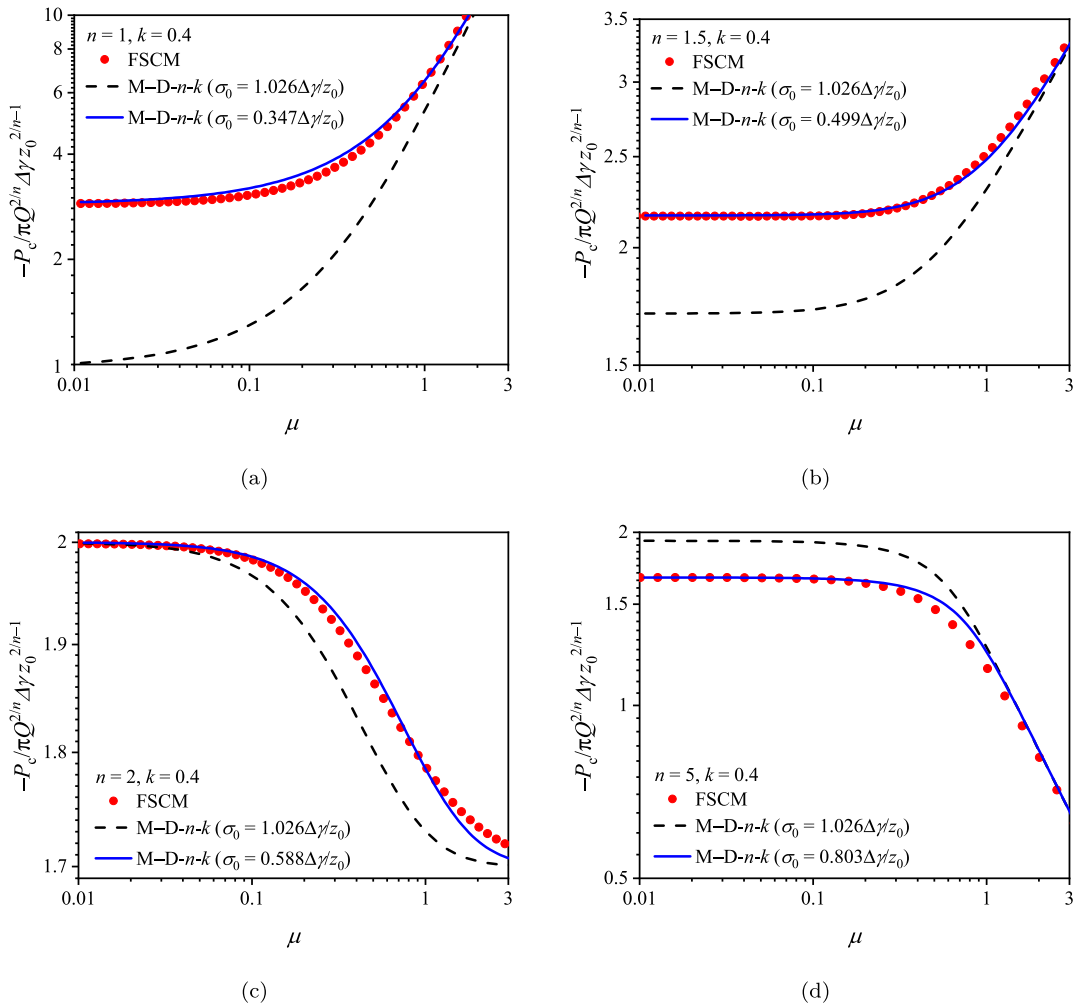
Fig. 14. Effect of the Tabor number on the pull-off force: comparison between the original and improved M–D-n-k models and the FSCM for (a) $n = 1$, (b) $n = 1.5$, (c) $n = 2$ and (d) $n = 5$ with $k = 0.4$.
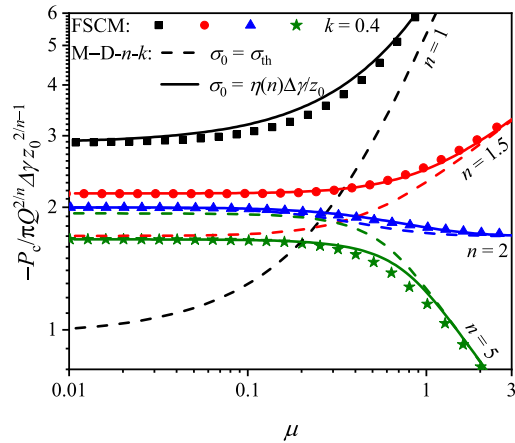

Fig. 15. Comparison of the JKR–Bradley transition between the original and improved M–D-n-k models and the FSCM with the pull-off force scaled by the rigid limit.
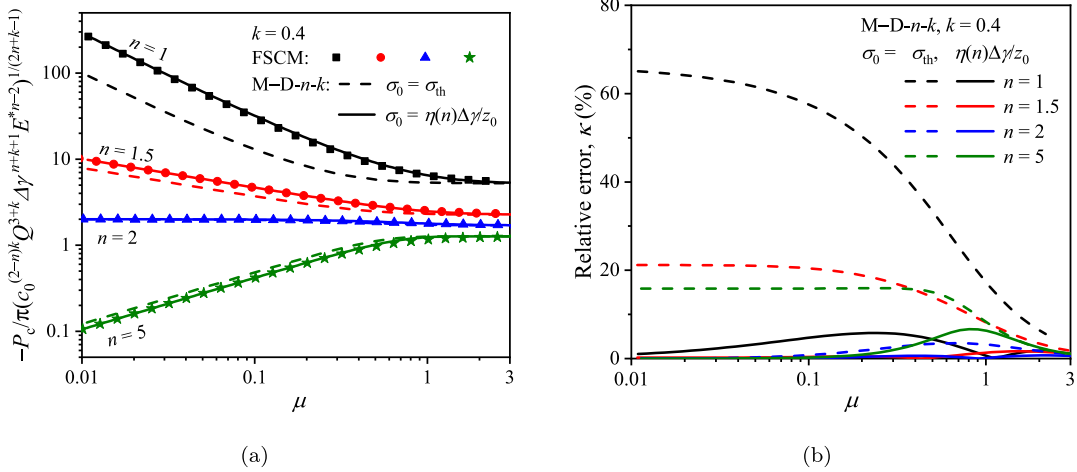
Fig. 16. (a) Comparison of the JKR–Bradley transition between the original and improved M–D-n-k models and the FSCM with the pull-off force scaled by the soft limit; (b) The relative errors between the M–D-n-k models and the FSCM.
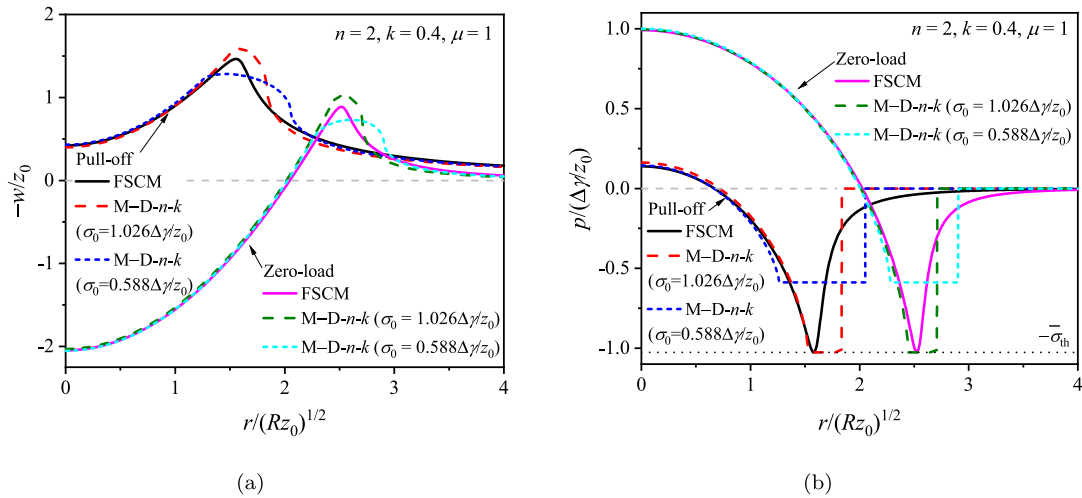

Fig. 17. Comparison between the original and improved M–D-n-k models and the FSCM: (a) the surface deformation and (b) the pressure distribution. Fixed parameters are $n = 2$, $k = 0.4$ and $\mu = 1$.

5. Conclusions

In this study, a full self-consistent model (FSCM) is developed for the adhesive contact between an axisymmetric rigid punch and a power-law graded elastic half-space. The adhesive contact problem is described by a nonlinear singular integral equation, which gives the coupling relationship between the surface gap and the surface interaction. With rigorous mathematical derivation, the singularity in numerical integration is eliminated through Riemann–Stieltjes integral. The power-law punch profiles are studied as representative cases and the surface interaction is described by the L–J force law. The self-consistent equation is nondimensionalized and its dimensionless form contains only three dimensionless parameters, i.e., the shape index n, the Tabor number μ, and the gradient exponent k. The surface central gap control method and Newton–Raphson iterative method are adopted to solve the nonlinear integral equation numerically, and the full force–displacement curves are obtained.

For a large Tabor number μ, the full force–displacement curve is 'S-shaped' and there are two unstable positions, namely the jumping-in/out points, if the displacement control method is adopted (e.g., in experimental tests). These phenomena were also observed in the homogeneous case (Greenwood, 1997; Feng, 2000). It is found that the JKR-n-k force–displacement curves coincide well with those of the FSCM at the high-load branch, but have a large difference at the low-load branch (including the jumping-in point) due to the absence of surface interaction before jumping-in contact in the JKR theory.

Asymptotic solutions are derived to predict the unstable positions during adhesive contact, which give power-law relations between the jumping-in/out displacements and the Tabor number. The dimensionless jumping-in displacement $\bar{\delta}^{\text{in}}$ is positively

correlated with $\mu^{(2n+k-1)/(4n+k-1)}$ and the dimensionless jumping-out displacement $\bar{\delta}^{\text{out}}$ is proportional to μ. The asymptotic solutions coincide well with the FSCM results and are useful in estimating the adhesion hysteresis energy loss of the power-law graded materials.

The effects of shape and material parameters on the adhesion of power-law graded materials are discussed in detail. With the increase of the Tabor number, the adhesion hysteresis becomes notable, and the dimensionless pull-off force increases for the small shape index (e.g., $n = 1$ and 1.5) and decreases for the large shape index (e.g., $n = 2$ and 5). The JKR–Bradley transition for the power-law graded material is obtained when the Tabor number increases from zero to infinity. There are two ranges for n ($0.974 \leq n \leq 1.056$ and $3.335 \leq n \leq 6.219$) where the relative deviation of the pull-off force between the graded and homogeneous materials is not sensitive to k. In these two ranges, the dimensionless pull-off force mainly depends on n and μ.

The FSCM is the most accurate adhesive contact model in the continuum framework, thus we apply it to validate the M–D-*n-k* model developed by Jin et al. (2021). It is shown that the accuracy of the original M–D-*n-k* model (Jin et al., 2021) is limited due to the improper choice of the cohesive stress. The M–D-*n-k* model is improved by applying *the rigid-limit-consistency condition* (Zheng and Yu, 2007b) to determine the value of the cohesive stress. Compared with the original M–D-*n-k* model, the improved one shows a much better agreement with the FSCM in many aspects, such as the force–displacement curves and the pull-off forces. Therefore, we strongly recommend *the rigid-limit-consistency condition* as an additional basic relation to the M–D-type models.

This study makes an attempt to establish a full self-consistent model for the adhesive contact of nonhomogeneous materials. It presents a further understanding on the adhesion of the power-law graded elastic materials and is helpful to verify/improve the existing simplified adhesive contact models. The FSCM for power-law graded materials developed in this study adopts the frictionless boundary condition, which may be further extended to the non-slipping adhesive contact cases, and the studies of the JKR and M–D type models (Chen and Gao, 2006a,b; Jin and Guo, 2010, 2012) may inspire this extension. For analytical tractability, the Young's modulus of graded materials considered in this work varies with depth according to a power-law relation and is zero at the surface. By combining with the adhesive contact solution of the homogeneous materials, the present results may provide a first approximation to the contact solution for power-law graded materials with non-zero surface modulus (Giannakopoulos and Pallot, 2000). The effect of surface modulus on the adhesion of power-law graded materials may be studied through a finite element method in the future.

CRediT authorship contribution statement

Yudong Zhu: Investigation, Methodology, Software, Validation, Formal analysis, Writing – original draft. **Zhijun Zheng:** Conceptualization, Methodology, Formal analysis, Supervision, Writing – review & editing, Funding acquisition, Data curation, Project administration. **Chenguang Huang:** Supervision, Writing – review & editing. **Jilin Yu:** Supervision, Writing – review & editing.

Declaration of competing interest

The authors declare that they have no known competing financial interests or personal relationships that could have appeared to influence the work reported in this paper.

Data availability

Data will be made available on request.

Acknowledgments

Appendix A. Some properties of the Gauss's hypergeometric function

The Gauss's hypergeometric function is defined as (Abramowitz and Stegun, 1965)

$$_2F_1(\alpha, \beta; \gamma; x) = \frac{\Gamma(\gamma)}{\Gamma(\beta)\Gamma(\gamma - \beta)} \int_0^1 \frac{t^{\beta-1}(1-t)^{\gamma-\beta-1}}{(1-xt)^\alpha} \, dt, \tag{A.1}$$

where $\Gamma(\cdot)$ is the Gamma function. In the following appendices, we abbreviate $_2F_1(\cdot)$ as $F(\cdot)$ for convenience. Some useful properties of the Gauss's hypergeometric function are given in this appendix and they will be used in the following Appendices. The following formulas can be consulted from the handbook of Abramowitz and Stegun (1965).

One of the Kummer's quadratic transformations is written as (Eq. 15.3.27 in p. 561 of Abramowitz and Stegun (1965))

$$F(\alpha, \beta; \alpha - \beta + 1; x^2) = (1+x)^{-2\alpha} F(\alpha, \alpha - \beta + \frac{1}{2}; 2\alpha - 2\beta + 1; \frac{4x}{(1+x)^2}). \tag{A.2}$$

The relations between the hypergeometric function and the complete elliptic integrals are given by (Eqs. 17.3.9 and 17.3.10 in p. 591 of Abramowitz and Stegun (1965))

$$K(x) = \frac{\pi}{2} F(\frac{1}{2}, \frac{1}{2}; 1; x^2),$$ (A.3)

$$E(x) = \frac{\pi}{2} F(-\frac{1}{2}, \frac{1}{2}; 1; x^2),$$ (A.4)

where $K(\cdot)$ and $E(\cdot)$ are the complete elliptic integrals. The derivative of $F(\alpha, \beta; \gamma; x)$ is given by (Eq. 15.2.1 in p. 557 of Abramowitz and Stegun (1965))

$$\frac{\mathrm{d}}{\mathrm{d}x} F(\alpha, \beta; \gamma; x) = \frac{\alpha\beta}{\gamma} F(\alpha + 1, \beta + 1; \gamma + 1; x).$$ (A.5)

Several Gauss's relations of the hypergeometric function are written as (Eqs. 15.2.10, 15.2.14, 15.2.18 and 15.2.20 in p. 557 of Abramowitz and Stegun (1965))

$$(\gamma - \alpha) F(\alpha - 1, \beta; \gamma; x) + (2\alpha - \gamma - \alpha x + \beta x) F(\alpha, \beta; \gamma; x) + \alpha (x - 1) F(\alpha + 1, \beta; \gamma; x) = 0,$$ (A.6)

$$(\beta - \alpha) F(\alpha, \beta; \gamma; x) + \alpha F(\alpha + 1, \beta; \gamma; x) - \beta F(\alpha, \beta + 1; \gamma; x) = 0,$$ (A.7)

$$(\gamma - \alpha - \beta) F(\alpha, \beta; \gamma; x) - (\gamma - \alpha) F(\alpha - 1, \beta; \gamma; x) + \beta (1 - x) F(\alpha, \beta + 1; \gamma; x) = 0,$$ (A.8)

$$\gamma (1 - x) F(\alpha, \beta; \gamma; x) - \gamma F(\alpha - 1, \beta; \gamma; x) + (\gamma - \beta) x F(\alpha, \beta; \gamma + 1; x) = 0.$$ (A.9)

Appendix B. Two special cases of Kummer's quadratic transformations

Taking $\alpha = \beta = (k + 1)/2$ and $x = r/t$ in Eq. (A.2) leads to

$$F(\frac{k + 1}{2}, \frac{k + 1}{2}; 1; \frac{r^2}{t^2}) = \frac{t^{k+1}}{(r + t)^{k+1}} F(\frac{k + 1}{2}, \frac{1}{2}; 1; \frac{4rt}{(r + t)^2}),$$ (B.1)

and making $\alpha = \beta = (k + 1)/2$ and $x = t/r$ in Eq. (A.2) gives

$$F(\frac{k + 1}{2}, \frac{k + 1}{2}; 1; \frac{t^2}{r^2}) = \frac{r^{k+1}}{(r + t)^{k+1}} F(\frac{k + 1}{2}, \frac{1}{2}; 1; \frac{4rt}{(r + t)^2}).$$ (B.2)

By using Eqs. (B.1) and (B.2), Eq. (6) can be rewritten as Eq. (8).

Appendix C. Two inferences of the Gauss's relations

Making $\alpha = \zeta$, $\beta = 1/2$ and $\gamma = 1$ in Eq. (A.7) yields

$$\frac{1}{2} (1 - 2\zeta) F(\zeta, \frac{1}{2}; 1; x) + \zeta F(\zeta + 1, \frac{1}{2}; 1; x) - \frac{1}{2} F(\zeta, \frac{3}{2}; 1; x) = 0.$$ (C.1)

Similarly, taking $\alpha = \zeta + 1$, $\beta = 1/2$ and $\gamma = 1$ in Eq. (A.8) leads to

$$-\frac{1}{2} (1 + 2\zeta) F(\zeta + 1, \frac{1}{2}; 1; x) + \zeta F(\zeta, \frac{1}{2}; 1; x) + \frac{1}{2} (1 - x) F(\zeta + 1, \frac{3}{2}; 1; x) = 0,$$ (C.2)

and considering $\alpha = \zeta + 1$, $\beta = 3/2$ and $\gamma = 1$ in Eq. (A.9) gives

$$(1 - x) F(\zeta + 1, \frac{3}{2}; 1; x) - F(\zeta, \frac{3}{2}; 1; x) - \frac{1}{2} x F(\zeta + 1, \frac{3}{2}; 2; x) = 0.$$ (C.3)

Then, substituting Eqs. (C.1) and (C.2) into Eq. (C.3), we have one inference of the Gauss's relations

$$F(\zeta + 1, \frac{3}{2}; 2; x) = \frac{2}{x} F(\zeta + 1, \frac{1}{2}; 1; x) - \frac{2}{x} F(\zeta, \frac{1}{2}; 1; x).$$ (C.4)

Replacing ζ with $\zeta + 1$ in Eq. (C.4) gives

$$F(\zeta + 2, \frac{3}{2}; 2; x) = \frac{2}{x} F(\zeta + 2, \frac{1}{2}; 1; x) - \frac{2}{x} F(\zeta + 1, \frac{1}{2}; 1; x),$$ (C.5)

and making $\alpha = \zeta + 1$, $\beta = 1/2$ and $\gamma = 1$ in Eq. (A.6) leads to

$$-\zeta F(\zeta, \frac{1}{2}; 1; x) + \frac{1}{2} (2\zeta + 1) (2 - x) F(\zeta + 1, \frac{1}{2}; 1; x) - (\zeta + 1) (1 - x) F(\zeta + 2, \frac{1}{2}; 1; x) = 0.$$ (C.6)

Thus, combining Eqs. (C.5) and (C.6), we have another inference of the Gauss's relations

$$F(\zeta + 2, \frac{3}{2}; 2; x) = \frac{1}{(\zeta + 1) x (1 - x)} \left[(2\zeta + x) F(\zeta + 1, \frac{1}{2}; 1; x) - 2\zeta F(\zeta, \frac{1}{2}; 1; x) \right].$$ (C.7)

Appendix D. Treatment of singular integral in the FSCM of homogeneous materials

The derivatives of $K(\cdot)$ and $E(\cdot)$ are

$$\frac{d}{ds}K(\frac{2\sqrt{s}}{1+s}) = \frac{1-s}{2s(1+s)}\left[-K(\frac{2\sqrt{s}}{1+s}) + \frac{(1+s)^2}{(1-s)^2}E(\frac{2\sqrt{s}}{1+s})\right],$$ (D.1)

$$\frac{d}{ds}E(\frac{2\sqrt{s}}{1+s}) = \frac{1-s}{2s(1+s)}\left[-K(\frac{2\sqrt{s}}{1+s}) + E(\frac{2\sqrt{s}}{1+s})\right].$$ (D.2)

Eqs. (D.1) and (D.2) give the relations between the complete elliptic integrals $E(\cdot)$, $K(\cdot)$ and their derivatives. By combining Eqs. (D.1) and (D.2), the term with $E(\cdot)$ on the right hand can be eliminated and we have

$$\frac{1}{\pi}\frac{d}{ds}\left[(s-1)K(\frac{2\sqrt{s}}{1+s}) + (1+s)E(\frac{2\sqrt{s}}{1+s})\right] = \frac{2s}{\pi(1+s)}K(\frac{2\sqrt{s}}{1+s}),$$ (D.3)

which corresponds to Eqs. (15) and (16). By using Eq. (D.3), Eq. (14) can be rewritten as Eq. (17), and the integral singularity at $s = 1$ (i.e., $t = r$) is eliminated.

Appendix E. Treatment of singular integral in the FSCM of graded materials

Inspired by the processing method in Appendix D, it is needed to find the primitive function of

$$\varphi_k(s) = \frac{s}{(1+s)^{k+1}}F(\frac{k+1}{2}, \frac{1}{2}; 1; \frac{4s}{(1+s)^2})$$ (E.1)

to eliminate the integral singularity at $t = r$ in Eq. (12). From Eq. (A.5), we can obtain the following derivative relations

$$\frac{d}{ds}F(\frac{k+1}{2}, \frac{1}{2}; 1; \frac{4s}{(1+s)^2}) = \frac{(k+1)(1-s)}{(1+s)^3}F(\frac{k+3}{2}, \frac{3}{2}, 2, \frac{4s}{(1+s)^2}),$$ (E.2)

$$\frac{d}{ds}F(\frac{k-1}{2}, \frac{1}{2}; 1; \frac{4s}{(1+s)^2}) = \frac{(k-1)(1-s)}{(1+s)^3}F(\frac{k+1}{2}, \frac{3}{2}, 2, \frac{4s}{(1+s)^2}).$$ (E.3)

Making use of Eqs. (C.7) and (C.4) with $\zeta = (k-1)/2$ and $x = 4s/(1+s)^2$, we can rewrite Eqs. (E.2) and (E.3) as

$$\frac{d}{ds}F(\frac{k+1}{2}, \frac{1}{2}; 1; \frac{4s}{(1+s)^2}) = \eta_1 F(\frac{k+1}{2}, \frac{1}{2}; 1; \frac{4s}{(1+s)^2}) + \eta_2 F(\frac{k-1}{2}, \frac{1}{2}; 1; \frac{4s}{(1+s)^2}),$$ (E.4)

$$\frac{d}{ds}F(\frac{k-1}{2}, \frac{1}{2}; 1; \frac{4s}{(1+s)^2}) = \eta_3 F(\frac{k+1}{2}, \frac{1}{2}; 1; \frac{4s}{(1+s)^2}) + \eta_4 F(\frac{k-1}{2}, \frac{1}{2}; 1; \frac{4s}{(1+s)^2}),$$ (E.5)

where η_1, η_2, η_3 and η_4 are given by

$$\eta_1 = \frac{k(1+s^2)}{s(1-s^2)} - \frac{(k+1)(1-s)}{2s(1+s)}, \quad \eta_2 = \frac{(1-k)(1+s)}{2s(1-s)}, \quad \eta_3 = \frac{(k-1)(1-s)}{2s(1+s)}, \quad \eta_4 = -\eta_3.$$ (E.6)

In fact, the term $1/(1+s)^k$ should also be included in the derivatives on the left side of Eqs. (E.4) and (E.5) to fully eliminate the primitive function $\varphi_k(s)$ for arbitrary values of k. From Eqs. (E.4) and (E.5), we have

$$\frac{d}{ds}\left[\frac{1}{(1+s)^k}F(\frac{k+1}{2}, \frac{1}{2}; 1; \frac{4s}{(1+s)^2})\right] = \eta_5 F(\frac{k+1}{2}, \frac{1}{2}; 1; \frac{4s}{(1+s)^2}) + \eta_6 F(\frac{k-1}{2}, \frac{1}{2}; 1; \frac{4s}{(1+s)^2}),$$ (E.7)

$$\frac{d}{ds}\left[\frac{1}{(1+s)^k}F(\frac{k-1}{2}, \frac{1}{2}; 1; \frac{4s}{(1+s)^2})\right] = \eta_7 F(\frac{k+1}{2}, \frac{1}{2}; 1; \frac{4s}{(1+s)^2}) + \eta_8 F(\frac{k-1}{2}, \frac{1}{2}; 1; \frac{4s}{(1+s)^2}),$$ (E.8)

where η_5, η_6, η_7 and η_8 are given by

$$\eta_5 = \frac{k(1+3s^2)-(1-s)^2}{2s(1-s)(1+s)^{k+1}}, \eta_6 = \frac{(1-k)(1+s)^2}{2s(1-s)(1+s)^{k+1}}, \eta_7 = \frac{(k-1)(1-s)}{2s(1+s)^{k+1}}, \eta_8 = \frac{1-s-k(1+s)}{2s(1+s)^{k+1}}.$$ (E.9)

Eqs. (E.7) and (E.8) give the relationships of two Gauss's hypergeometric functions and their derivatives. Combining Eqs. (E.7) and (E.8) to eliminate the term with $F((k-1)/2, 1/2; 1; 4s/(1+s)^2)$ on the right hand, we have

$$\frac{d}{ds}\left[\frac{s-1}{2(1+s)^k}F(\frac{k+1}{2}, \frac{1}{2}; 1; \frac{4s}{(1+s)^2}) + \frac{1+s}{2(1+s)^k}F(\frac{k-1}{2}, \frac{1}{2}; 1; \frac{4s}{(1+s)^2})\right] = (1-k)\varphi_k(s).$$ (E.10)

This relation leads to Eqs. (18) and (19), and the singular point at $s = 1$ (i.e., $t = r$) for power-law graded elastic materials is eliminated.

References

Abramowitz, M., Stegun, I.A., 1965. Handbook of Mathematical Functions with Formulas, Graphs, and Mathematical Tables. US Government printing office.

Arzt, E., Gorb, S., Spolenak, R., 2003. From micro to nano contacts in biological attachment devices. Proc. Natl. Acad. Sci. USA 100, 10603–10606.

Attard, P., Parker, J.L., 1992. Deformation and adhesion of elastic bodies in contact. Phys. Rev. A 46, 7959–7971.

Barber, J.R., 2018. Contact Mechanics. Springer International Publishing, Berlin.

Booker, J.R., Balaam, N.P., Davis, E.H., 1985a. The behaviour of an elastic non-homogeneous half-space, Part I–line and point loads. Int. J. Numer. Anal. Methods Geomech. 9, 353–367.

Booker, J.R., Balaam, N.P., Davis, E.H., 1985b. The behaviour of an elastic non-homogeneous half-space, Part II–circular and strip footings. Int. J. Numer. Anal. Methods Geomech. 9, 369–381.

Bradley, R.S., 1932. The cohesive force between solid surfaces and the surface energy of solids. Lond. Edinb. Dublin Philos. J. Sci. 13, 853–862.

Chen, S., Gao, H., 2006a. Non-slipping adhesive contact between mismatched elastic spheres: a model of adhesion mediated deformation sensor. J. Mech. Phys. Solids 54, 1548–1567.

Chen, S., Gao, H., 2006b. Generalized Maugis–Dugdale model of an elastic cylinder in non-slipping adhesive contact with a stretched substrate. Int. J. Mater. Res. 97, 584–593.

Chen, S., Yan, C., Soh, A., 2009a. Adhesive behavior of two-dimensional power-law graded materials. Int. J. Solids. Struct. 46, 3398–3404.

Chen, S., Yan, C., Zhang, P., Gao, H., 2009b. Mechanics of adhesive contact on a power-law graded elastic half-space. J. Mech. Phys. Solids 57, 1437–1448.

Ciavarella, M., Greenwood, J.A., Barber, J.R., 2017. Effect of Tabor parameter on hysteresis losses during adhesive contact. J. Mech. Phys. Solids 98, 236–244.

Derjaguin, B.V., 1934. Theorie des anhaftens kleiner teilchen (theory of adhering small particles). Kolloidn. Zh. 69, 155–164.

Derjaguin, B.V., Muller, V.M., Toporov, Y.P., 1975. Effect of contact deformations on the adhesion of particles. J. Colloid Interface Sci. 53, 314–326.

Dong, X., Zhang, R., Tian, Y., Ramos, M.A., Hu, T.S., Wang, Z., Zhao, H., Zhang, L., Wan, Y., Xia, Z., Xu, Q., 2020. Functionally graded gecko setae and the biomimics with robust adhesion and durability. ACS Appl. Polym. Mater. 2, 2658–2666.

Feng, J.Q., 2000. Contact behavior of spherical elastic particles: a computational study of particle adhesion and deformations. Colloids Surf. A 172, 175–198.

Flenner, S., Schaber, C.F., Krasnov, I., Stieglitz, H., Rosenthal, M., Burghammer, M., Gorb, S.N., Müller, M., 2020. Multiple mechanical gradients are responsible for the strong adhesion of spider attachment hair. Adv. Mater. 2002758.

Gao, H., Yao, H., 2004. Shape insensitive optimal adhesion of nanoscale fibrillar structures. Proc. Natl. Acad. Sci. USA 101, 7851–7856.

Giannakopoulos, A.E., Pallot, P., 2000. Two-dimensional contact analysis of elasticgraded materials. J. Mech. Phys. Solids 48, 1597–1631.

Giannakopoulos, A.E., Suresh, S., 1997a. Indentation of solids with gradients in elastic properties: Part I. Point force. Int. J. Solids Struct. 34, 2357–2392.

Giannakopoulos, A.E., Suresh, S., 1997b. Indentation of solids with gradients in elastic properties: Part II. Axisymmetric indenters. Int. J. Solids Struct. 34, 2393–2428.

Goryacheva, I.G., Makhovskaya, Y.Y., 2001. Adhesive interaction of elastic bodies. J. Appl. Math. Mech. 65, 273–282.

Greenwood, J.A., 1997. Adhesion of elastic spheres. Proc. R. Soc. Lond. Ser. A Math. Phys. Eng. Sci. 453, 1277–1297.

Greenwood, J.A., 2007. On the DMT theory. Tribol. Lett. 26, 203–211.

Greenwood, J.A., 2009. Adhesion of small spheres. Philos. Mag. 89, 945–965.

Greenwood, J.A., Johnson, K.L., 1998. An alternative to the Maugis model of adhesion between elastic spheres. J. Phys. D: Appl. Phys. 31, 3279–3290.

Grierson, D.S., Liu, J., Carpick, R.W., Turner, K.T., 2013. Adhesion of nanoscale asperities with power-law profiles. J. Mech. Phys. Solids 61 (2), 597–610.

Guo, X., Jin, F., Gao, H., 2011. Mechanics of non-slipping adhesive contact on a power-law graded elastic half-space. Int. J. Solids. Struct. 48, 2565–2575.

Hertz, H., 1882. Über die Berührung fester elastischer Körper (on the contact of elastic solids). J. Reine Angew. Math. 92, 156–171.

Hughes, B.D., White, L.R., 1979. 'Soft' contact problems in linear elasticity. Q. J. Mech. Appl. Math. 32, 445–471.

Jin, F., Guo, X., 2010. Non-slipping adhesive contact of a rigid cylinder on an elastic power-law graded half-space. Int. J. Solids Struct. 47, 1508–1521.

Jin, F., Guo, X., 2012. Mode-mixity-dependent adhesion of power-law graded elastic solids under normal and substrate stretch-induced mismatch strain. Int. J. Solids Struct. 49, 2349–2357.

Jin, F., Guo, X., 2013. Mechanics of axisymmetric adhesive contact of rough surfaces involving power-law graded materials. Int. J. Solids Struct. 50, 3375–3386.

Jin, F., Guo, X., Gao, H., 2013. Adhesive contact on power-law graded elastic solids: The JKR–DMT transition using a double-Hertz model. J. Mech. Phys. Solids 61, 2473–2492.

Jin, F., Guo, X., Wan, Q., 2018. Plane contact and adhesion of two elastic solids with an interface groove. J. Appl. Mech. 85, 041002-1–041002-10.

Jin, F., Tang, Q., Guo, X., Gao, H., 2021. A generalized Maugis-Dugdale solution for adhesion of power-law graded elastic materials. J. Mech. Phys. Solids 154, 104509.

Jin, F., Zhang, W., Wan, Q., Guo, X., 2016. Adhesive contact of a power-law graded elastic half-space with a randomly rough rigid surface. Int. J. Solids Struct. 81, 244–249.

Johnson, K.L., Greenwood, J.A., 1997. An adhesion map for the contact of elastic spheres. J. Colloid Interface Sci. 192, 326–333.

Johnson, K.L., Greenwood, J.A., 2008. Maugis analysis of adhesive line contact. J. Phys. D: Appl. Phys. 41, 155315-1–155315-6.

Johnson, K.L., Kendall, K., Roberts, A.D., 1971. Surface energy and contact of elastic solids. Proc. R. Soc. London A 324, 301–313.

Li, Q., Popov, V.L., 2018. Boundary element method for normal non-adhesive and adhesive contacts of power-law graded elastic materials. Comput. Mech. 61, 319–329.

Maugis, D., 1992. Adhesion of spheres: the JKR–DMT transition using a Dugdale model. J. Colloid Interface Sci. 150, 243–269.

Muller, V.M., Yushchenko, V.S., Derjaguin, B.V., 1980. On the influence of molecular forces on the deformation of an elastic sphere and its sticking to a rigid plane. J. Colloid Interface Sci. 77, 91–101.

Papangelo, A., Ciavarella, M., 2020. A numerical study on roughness-induced adhesion enhancement in a sphere with an axisymmetric sinusoidal waviness using Lennard–Jones interaction law. Lubricants 8 (9), 90.

Song, Z., Komvopoulos, K., 2014. Adhesive contact of an elastic semi-infinite solid with a rigid rough surface: strength of adhesion and contact instabilities. Int. J. Solids Struct. 51, 1197–1207.

Tabor, D., 1977. Surface forces and surface interactions. J. Colloid Interface Sci. 58, 2–13.

Willert, E., 2018. Dugdale-Maugis adhesive normal contact of axisymmetric power-law graded elastic bodies. Facta Univers. Ser. Mech. Eng. 16, 9–18.

Wu, J.J., 2009. Adhesive contact between a cylinder and a half-space. J. Phys. D: Appl. Phys. 42, 155302-1–155302-8.

Wu, J.J., 2010. The jump-to-contact distance in atomic force microscopy measurement. J. Adhes. 86, 1071–1085.

Yao, H., Gao, H., 2007. Mechanical principles of robust and releasable adhesion of gecko. J. Adhes. Sci. Tech. 21, 1185–1212.

Zheng, Z., Yu, J.L., 2007a. A generalized Maugis model for adhesive contact of arbitrary axisymmetric elastic objects. Chin. J. Theor. Appl. Mech. 39, 382–388, (in Chinese).

Zheng, Z., Yu, J., 2007b. Using the Dugdale approximation to match a specific interaction in the adhesive contact of elastic objects. J. Colloid Interface Sci. 310, 27–34.

Zheng, Z.J., Yu, J.L., Li, J., Lin, J.R., 2007. Adhesive contact of power-law axisymmetric elastic objects. J. Univ. Sci. Tech. CHN 37, 1293–1299, (in Chinese).

Zhou, S., Gao, X., He, Q., 2011. A unified treatment of axisymmetric adhesive contact problems using the harmonic potential function method. J. Mech. Phys. Solids 59, 145–159.

Zhu, Y.D., Zheng, Z.J., Zhang, Y.L., Wu, H.A., Yu, J.L., 2021. Adhesion of elastic wavy surfaces: Interface strengthening/weakening and mode transition mechanisms. J. Mech. Phys. Solids 151, 104402.